

MEASURING THE MUONIC DECAY OF THE D^+
MESON USING NEUTRINO RECONSTRUCTION.

A Dissertation

Presented to the Faculty of the Graduate School

of Cornell University

in Partial Fulfillment of the Requirements for the Degree of

Doctor of Philosophy

by

Daniel Braddock Hertz

January 2009

This document is in the public domain.

MEASURING THE MUONIC DECAY OF THE D^+ MESON USING
NEUTRINO RECONSTRUCTION.

Daniel Braddock Hertz, Ph.D.

Cornell University 2009

Using 281 pb^{-1} of data collected at the $\psi(3770)$ resonance at the CLEO-c detector, we measure the purely leptonic decay of the D^+ meson using the channel $D^+ \rightarrow \mu^+ \nu_\mu$. We use a method which takes advantage of the intrinsic hermeticity of the CLEO-c detector in order to reconstruct the missing momentum and energy, which is then interpreted as the signal neutrino. The resolution of the missing energy is improved by fully reconstructing the hadronically decaying D meson as a combination of $\pi^\pm, K^\pm, K_S \rightarrow \pi^+ \pi^-, \pi^0 \rightarrow \gamma\gamma$ and $\eta \rightarrow \gamma\gamma$. Low energy showers which cannot be associated with $\pi^0 \rightarrow \gamma\gamma$ or $\eta \rightarrow \gamma\gamma$ are rejected. By replacing the signal leptonic decay channel with a well measured D^+ hadronic decay such as $D^+ \rightarrow K^- \pi^+ \pi^+$ and requiring the missing energy to be small, we can use the same generic reconstruction technique to measure systematic errors that may affect the overall efficiency of the leptonic analysis. In order to reduce our systematic errors, we scale our leptonic yields by the $D^+ \rightarrow K^- \pi^+ \pi^+$ yield and find the branching fraction in terms of the $D^+ \rightarrow K^- \pi^+ \pi^+$ branching fraction. We find $\mathcal{B}(D^+ \rightarrow \mu^+ \nu_\mu) = (3.90 \pm 0.55_{stat} \pm 0.13_{syst}) \times 10^{-4}$ for the branching fraction of the process, from which we extract $f_{D^+} = (209.7 \pm 14.6_{stat} \pm 3.5_{syst}) \text{ MeV}$.

BIOGRAPHICAL SKETCH

Daniel Hertz was born in Evanston, IL in 1978 and moved to Denmark in August of 1980, where he spent most of his youth. He attended primary and secondary education at Danish schools and is thus both fluent in the Danish language and knowledgeable about important historical events such as the collectivization movement of Danish agriculture in the 19th century. During his secondary school years he delivered newspapers every morning before school, preparing him for later curmudgeonhood by giving him excellent source material for stories beginning with the phrase “when I was your age. . .”

He decided that going to an English-speaking university would be preferable to staying in Denmark and he therefore attended Merton College, Oxford University, where he studied physics and rowed in the college 1st VIII. Arriving at Cornell in 2000 for physics graduate school, he took a leave of absence for the academic year 2001-2002 during which time he taught for the physics department. Returning with the ultimate intention of teaching, he started working in the HEP group and found the research to be even more interesting than he had imagined it might be; Dan spent several years in the depths of Wilson lab working on the High Voltage system and drift chamber electronics and serving as an assistant run manager for CLEO. He now hopes to apply the skills he has learned in particle physics to the field of neuroscience.

This work is dedicated to the memory of Dr. Jean-Etienne Duboscq, my office mate and great friend for all of my time at Wilson Lab. His constant helpful advice, not only about physics but life in general helped keep me sane during my tenure there.

ACKNOWLEDGEMENTS

First and foremost I wish to thank my wife Beth for her constant support during the extended period of time I spent working on this analysis, much of which took place while we were living in separate cities. I would also like to thank Jim Alexander, my advisor, for guiding me through much of this process and indeed for helping to bring me back into physics after my leave of absence; without him I would not be here today. This analysis in its present form would not exist without the work of Richard Gray, for which I am extremely grateful, and I am also deeply indebted to a number of other Cornell graduate students, chiefly Peter Onyisi, Steve Stroiney, Laura Fields and Xin Shi, for help at various points. Much of the initial neutrino reconstruction framework was laid down by Tom Meyer and Nadia Adam, the latter of whom spent quite a bit of time explaining its workings to me. The Rochester group at CLEO is also owed many thanks, in particular Ed Thorndike and Chul Su Park, who got me involved in my first set of analyses as well as keeping an eye on my continuing progress.

I owe a tremendous debt of gratitude to the various software experts at CLEO, principally Werner Sun, Chris Jones and Brian Heltsley, as well as the software coordinators Dave Kreinick, Istvan Danko and Pete Zweber, who all patiently put up with my various odd requests for extra Monte Carlo and disk space. Special thanks also go to Hanna Mahlke and Brian Heltsley for assistance with radiative returns, and Hajime Muramatsu for discussions regarding the continuum.

Finally, I must thank the staff at CESR for providing the luminosity to allow us to take the data at CLEO. Further, I wish to thank the rest of the hardware group at CLEO, particularly the run managers I've worked with: Basit Athar, Topher Caulfield and Ji Li.

TABLE OF CONTENTS

Biographical Sketch	iii
Dedication	iv
Acknowledgements	v
Table of Contents	vi
List of Tables	viii
List of Figures	ix
1 Introduction	1
1.1 Quarks	1
1.2 Lattice QCD	3
1.3 The Simplest Decay	7
1.4 CLEO-c and f_{D^+}	10
2 The CLEO-c Detector	12
2.1 Detector Overview	12
2.2 Drift Chambers	12
2.2.1 Inner Stereo Drift Chamber: ZD	14
2.2.2 Main Drift Chamber: DR	14
2.3 Ring Imaging Cherenkov Detector: RICH	15
2.4 Electromagnetic Calorimeter: CC	17
2.5 Muon Detectors	19
3 Event Reconstruction	20
3.1 Overview	20
3.2 Trkman	21
3.3 Splitoff	23
3.4 Initial Neutrino Reconstruction	25
3.4.1 ΔE	27
3.4.2 M_{BC}	28
3.5 Improved Neutrino Reconstruction	29
3.6 μ^+ Candidate Properties	33
3.7 $\Delta E_{o.s.}$	36
3.8 $MM_{s.s.}^2$	36
3.9 m_{ν^2}	39
3.10 Other Criteria	40
3.11 Summary of Selection Criteria	43
4 Reconstruction Efficiency and the D Hadronic Branching Fractions	45
4.1 Why do we need to know the Hadronic Branching Fractions?	45
4.2 Method	47
4.3 Counting $D\bar{D}$ pairs	50
4.4 Measured Efficiency	50

5	Backgrounds	51
5.1	Overview	51
5.2	$e^+e^- \rightarrow q\bar{q}$: Continuum Production to Light quarks	51
5.3	$e^+e^- \rightarrow \psi'\gamma$: Radiative Returns	55
5.4	$e^+e^- \rightarrow \tau^+\tau^-$: τ -Pair Production	58
5.5	$D\bar{D}$ -Pairs	61
5.5.1	$D^+ \rightarrow \pi^+K_L$	65
5.5.2	$D^+ \rightarrow \pi^+\pi^0$	68
5.5.3	$D^+ \rightarrow \tau^+\nu_\tau$	69
6	Fitting	73
6.1	Overview	73
6.2	Signal Fitting	73
6.3	Background Fitting	74
6.3.1	$e^+e^- \rightarrow \psi'\gamma$ and $\tau^+\tau^-$	75
6.3.2	$D\bar{D}$ -pairs	76
6.3.3	$D^+ \rightarrow \pi^+K_L$	76
6.3.4	$D^+ \rightarrow \pi^+\pi^0$ and $D^+ \rightarrow \tau^+\nu_\tau$	77
6.3.5	Continuum	78
6.4	Combined Fit	81
6.5	Fitting $D \rightarrow K^-\pi^+\pi^+$	83
7	Systematic Uncertainties	86
7.1	Overview	86
7.2	Corrections	86
7.3	Fitting	87
7.4	Selection Requirements	87
7.5	Tracking	89
7.6	Hadronic Branching Fraction Ratio	89
7.7	Summary	89
8	Results	91
	Bibliography	92

LIST OF TABLES

3.1	Event Selection Criteria	42
6.1	The parameters for the fit to the signal Monte Carlo, used to determine the shape of the signal peak in the final fit.	74
6.2	The parameters for all the different fitted portions of the background, obtained from Monte Carlo.	80
6.3	The parameters for the continuum ARGUS fit and the signal peak yield obtained from the fit to data.	81
6.4	The parameters for the $D^+ \rightarrow K^- \pi^+ \pi^+$ fit from data.	84
7.1	Systematic Uncertainties	89
8.1	The efficiency corrected yields for $D^+ \rightarrow K^- \pi^+ \pi^+$ and $D^+ \rightarrow \mu^+ \nu_\mu$	91

LIST OF FIGURES

1.1	A simple example of a lattice of size L with spacing a . The action at adjacent sites is linked (from [1]).	4
1.2	A series of predictions from unquenched lattice QCD, and their earlier counterparts (from [2]).	5
1.3	The Feynmann diagram for the purely leptonic decay of the D^+ meson.	8
2.1	A cutaway view of the CLEO-c detector showing its chief components.	13
2.2	A schematic representation of the RICH detector in CLEO-c. . . .	16
2.3	A side view of the CLEO detector, showing the angling of the CC crystals. This also shows the relative positioning of the ZD, DR, RICH and CC detectors.	18
3.1	An event from data showing a $D^+ \rightarrow \mu^+ \nu_\mu$ event containing a curler.	22
3.2	An representation of a split-off. The image is from [3]	24
3.3	The $\Delta E_{s.s.}$ distribution for signal Monte Carlo (MC) events before any cuts are made.	28
3.4	The pull mass distribution for Monte Carlo truth π^0 's.	31
3.5	Mass resolution of MC truth π^0 's	31
3.6	Mass resolution of MC truth $\eta \rightarrow \gamma\gamma$'s	32
3.7	$\Delta E_{o.s.}$ for signal Monte Carlo without (black points) and with (solid red histogram) the improved other side shower reconstruction. . . .	33
3.8	Energy deposited in the calorimeter by the μ^+ candidate track for signal Monte Carlo.	35
3.9	Energy deposited in the calorimeter by the μ^+ candidate track for $D^+ \rightarrow \pi^+ \pi^0$ Monte Carlo where the μ^+ candidate is in fact a π^+ . .	35
3.10	$\Delta E_{o.s.}$ for signal Monte Carlo with loose selection requirements. The tail on the left is dominated by lost showers.	37
3.11	$MM_{s.s.}^2$ for signal Monte Carlo (with only loose selection criteria). The tails of the distribution are from cases where the event is not reconstructed properly because of additional neutrinos, K_L 's or lost showers.	38
3.12	$MM_{s.s.}^2$ for $D^+ \rightarrow \pi^+ K_L$	39
3.13	$\Delta E_{s.s.}$ for $D^+ \rightarrow \pi^+ K_L$	39
3.14	Total vetoed shower energy for signal Monte Carlo (with only loose selection criteria). Note that the majority of events have only a very small vetoed energy—nowhere near our cutoff of 300 MeV. . .	41
3.15	M_{BC} for signal Monte Carlo with only very loose cuts. The tails are caused by poor ν reconstruction.	42
3.16	M_{BC} for signal Monte Carlo after all selection cuts.	43
5.1	Distribution of $\cos\theta$ of \vec{p}_{miss} for continuum MC. Note the very strong peaking towards ± 1	53

5.2	$\Delta E_{\text{o.s.}}$ for continuum MC with very loose cuts; there is no narrow peaking structure.	54
5.3	$MM_{\text{s.s.}}^2$ for continuum MC with very loose cuts; there is no narrow peaking structure.	54
5.4	M_{BC} for continuum MC with only very loose cuts. Note the basic ARGUS shape.	55
5.5	M_{BC} for continuum MC which has passed our selection criteria. . .	55
5.6	Distribution of $\cos\theta$ of \vec{p}_{miss} for radiative return MC. This peaks strongly towards ± 1	56
5.7	$\Delta E_{\text{o.s.}}$ for radiative returns Monte Carlo.	57
5.8	$MM_{\text{s.s.}}^2$ for radiative returns Monte Carlo.	57
5.9	M_{BC} for radiative return MC before cuts.	58
5.10	M_{BC} for radiative return MC after cuts.	58
5.11	Distribution of $\cos\theta$ of \vec{p}_{miss} for τ -pair MC. Note that it does not peak towards ± 1	59
5.12	$\Delta E_{\text{o.s.}}$ for τ -pair MC without cuts. There are neutrinos in the decays on <i>both</i> sides of the event, so there will be less energy left over to create a D^- -candidate, hence the shape of this plot.	60
5.13	$MM_{\text{s.s.}}^2$ for τ -pair MC without cuts. The shape is created by the presence of multiple ν 's in the event.	60
5.14	M_{BC} for τ -pair MC before our event selection criteria.	61
5.15	M_{BC} for τ -pair MC after our event selection criteria.	61
5.16	Distribution of $\cos\theta$ of \vec{p}_{miss} for generic $D\bar{D}$ MC. It also peaks towards the direction of the beam pipe because of lost particles and showers.	63
5.17	$MM_{\text{s.s.}}^2$ for 'generic' $D\bar{D}$ MC with the loosest possible cuts. There is no real structure other than a monotonic increase towards higher $MM_{\text{s.s.}}^2$	63
5.18	$\Delta E_{\text{o.s.}}$ for 'generic' $D\bar{D}$ MC with the loosest possible cuts. There is no real structure other than a monotonic increase towards higher $\Delta E_{\text{o.s.}}$	64
5.19	M_{BC} for generic $D\bar{D}$ MC before our event selection criteria.	64
5.20	M_{BC} for generic $D\bar{D}$ MC after our event selection criteria.	65
5.21	$\Delta E_{\text{o.s.}}$ for $D^+ \rightarrow \pi^+ K_L$ MC with the loosest possible cuts; the other side is well reconstructed for these events.	66
5.22	$MM_{\text{s.s.}}^2$ for $D^+ \rightarrow \pi^+ K_L$ MC with the loosest possible cuts. Note the large peak at $0.25 \text{ GeV}^2/c^4$, the K_L mass.	66
5.23	M_{BC} for $D^+ \rightarrow \pi^+ K_L$ MC with the loosest possible cuts; it looks very like signal.	67
5.24	M_{BC} for $D^+ \rightarrow \pi^+ K_L$ MC with all our selection cuts; it now has a complex shape.	67
5.25	$\Delta E_{\text{o.s.}}$ for $D^+ \rightarrow \pi^+ \pi^0$ MC with loose cuts. there are large broader tails than for signal MC.	68

5.26	$MM_{\text{s.s.}}^2$ for $D^+ \rightarrow \pi^+\pi^0$ MC with the loosest possible cuts. Note the peaks at both 0.02 and 0.25 GeV^2/c^4	69
5.27	M_{BC} for $D^+ \rightarrow \pi^+\pi^0$ MC with all our cuts; it looks just like signal.	70
5.28	$\Delta E_{\text{o.s.}}$ for $D^+ \rightarrow \tau^+\nu_\tau$ MC with the loosest possible cuts; it looks exactly like signal MC.	71
5.29	M_{BC} for $D^+ \rightarrow \tau^+\nu_\tau$ MC with the loosest possible cuts, resembling signal MC.	71
5.30	M_{BC} for $D^+ \rightarrow \tau^+\nu_\tau$ MC after all cuts, greatly diminished in magnitude.	72
5.31	$MM_{\text{s.s.}}^2$ for $D^+ \rightarrow \tau^+\nu_\tau$ MC with the loosest possible cuts. The peak is broadly smeared from zero in the positive direction.	72
6.1	A fit of the signal Monte Carlo to a sum of two Gaussians.	74
6.2	A fit of the $e^+e^- \rightarrow \psi'\gamma$ Monte Carlo to an ARGUS function.	75
6.3	A fit of the $e^+e^- \rightarrow \tau^+\tau^-$ Monte Carlo to an ARGUS function.	76
6.4	A fit of the generic $D\bar{D}$ -pairs Monte Carlo using an ARGUS function.	77
6.5	A fit of the $D^+ \rightarrow \pi^+K_L$ Monte Carlo using a Gaussian plus an ARGUS function.	78
6.6	A fit of the $D^+ \rightarrow \pi^+\pi^0$ Monte Carlo using two Gaussians.	79
6.7	A fit of the $D^+ \rightarrow \tau^+\nu_\tau$ Monte Carlo using two Gaussians.	79
6.8	A fit of data using the combined information from the backgrounds and signal. In ascending order, the contributions are: $D\bar{D}$ (green dashed) $e^+e^- \rightarrow \psi'\gamma$ (orange solid), $e^+e^- \rightarrow \tau^+\tau^-$ (gray dashed), continuum (blue solid), $D^+ \rightarrow \pi^+K_L$ (purple dashed), $D^+ \rightarrow \pi^+\pi^0$ (yellow solid) and signal peak (red solid).	82
6.9	A fit of data using the combined information from the backgrounds and signal. To help illustrate the background components, the y -axis is logarithmic. In ascending order, the contributions are: $D\bar{D}$ (green dashed) $e^+e^- \rightarrow \psi'\gamma$ (orange solid), $e^+e^- \rightarrow \tau^+\tau^-$ (gray dashed), continuum (blue solid), $D^+ \rightarrow \pi^+K_L$ (purple dashed), $D^+ \rightarrow \pi^+\pi^0$ (yellow solid) and signal peak (red solid).	83
6.10	A fit to data of the $D^+ \rightarrow K^-\pi^+\pi^+$ reference mode, as a combination of an ARGUS background plus a signal peak which is the sum of a Gaussian and a Crystal Ball function.	84

Chapter 1

Introduction

1.1 Quarks

Three quarks for Muster Mark!
Sure he hasn't got much of a bark
And sure any he has it's all beside the mark.
– James Joyce, *Finnegans Wake* [4]

When Murray Gell-Mann first suggested the name “quark” for the fundamental building blocks of hadrons, it was perhaps with more foresight than may typically be credited. There are indeed more than the three flavors he knew of at the time, but there are three generations of quarks, and they interact via the strong interaction where they carry one of three “color charges”. Gell-Mann himself claimed that one of the name’s virtues is that, because it has no inherent meaning, it cannot become obsolete; this being in rather stark contrast to a great many words chosen by particle physicists, such as lepton, hadron, meson and proton to name but a few. Furthermore, its lack of connotations means that it is unfettered by preconceived associations with the classical world; this again stands in contrast to the choice of words such as “color” to help describe Quantum **Chrom**odynamics (QCD), or indeed the names given to the different quark flavors (up, down, charm, strange, top, bottom). Perhaps wiser choices for those terms would have been to borrow from other literary sources such as *Jabberwocky* [5], giving us “mimsy” “manxome” and “vorpal” quarks so as to free us from associations with “charm” and “strangeness” in particle physics. However, it seems that we are stuck with

our existing terms and must learn to live with them.

But what *is* a quark? A basic answer would be that it is a fundamental elementary fermion, carrying angular momentum, electromagnetic, color and weak hypercharge. The color charges come, as mentioned, in one of three types: red, green and blue. The electric charge is either $+\frac{2}{3}e$ (for up, charm and top) or $-\frac{1}{3}e$ (for down, strange and bottom). The defining aspect of quarks, perhaps, is the fact that they are never seen singly, but must always be found either in quark-antiquark pairs (in mesons) or in groups of three quarks or antiquarks (in baryons). This ensures that fractionally electrically charged particles and color charged particles are never observed. The mechanism by which they are bound to each other in this manner is known as *asymptotic freedom* and lies well beyond the scope of this treatise. Suffice it to say that quarks are indeed confined to exist only in mesons and baryons. Their mutual attraction is mediated by gluons, which act as the force carrier of the strong force, and which ensure that the quarks remain confined. They also ensure that calculations regarding these quarks remain very difficult because of their self-interaction: not only do gluons interact with quarks, they also interact with each other, and thus a whole new level of complexity is added to the mix. This stands in contrast to the electromagnetic force, where the photon does not carry electromagnetic charge itself, of course; as a result, photons only interact very weakly with themselves, through loop diagrams, while gluons do so at tree level.

The fact that the gluons interact with themselves and each other as well as the quarks makes drawing any kind of Feynmann diagram for strong interactions very difficult at low energy. At high energy, asymptotic freedom means that these interactions are fairly straightforward to calculate, and indeed for interactions that

occur at the LHC, it would indeed be possible to draw Feynmann diagrams for the interactions. However, for low-energy calculations it is not useful to draw the leading order (LO) diagrams, and then the next to leading order (NLO) diagrams, and then the next to next to leading order (NNLO), and so forth. The reason is that, Unlike for QED (or for QCD when one is approaching asymptotic freedom) the contribution from these diagrams won't actually be getting smaller in any convergent sort of way. If we are to make any kind of attempt at calculating things with QCD, we are going to need some other kind of approach. It is obviously also the case that if we are to have any understanding of the structure of mesons, for instance, we need to have some understanding of QCD. We can get this purely from experiment, of course, but if we are unable to test the accuracy of QCD, how are we to verify it? Fortunately, in recent years there has emerged a technique that allows for some QCD calculations at low energies by quantizing space and time on to a lattice.

1.2 Lattice QCD

The approach of Lattice QCD (LQCD) is to say that the problem of QCD is indeed too difficult to solve *analytically* at low energies. The answer will therefore to be to solve it in a brute-force fashion by doing it *numerically*. While this may sound simple it is in fact anything but. The idea is to discretize time and space by calculating the QCD action at different points in space-time on a lattice, an example of which is shown in Figure 1.1. By performing this calculation on a series of different lattices with coarser and finer spacings, one can determine what the continuum limit result of the same calculation would be. Actually calculating path integrals in this manner is obviously enormously CPU-intensive and requires

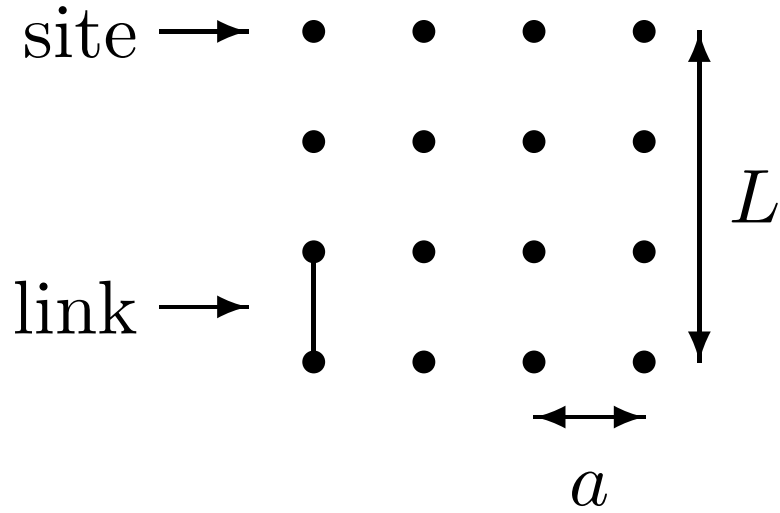


Figure 1.1: A simple example of a lattice of size L with spacing a . The action at adjacent sites is linked (from [1]).

a number of tricks in order to work properly. It is only in the past four years that the tools have come into existence which have allowed for the calculation of real quantities using this technique. Prior to that time, all calculations made were what is called “quenched” lattice calculations. These had to, in order to be able to run in a realistic amount of time, make some unfortunate assumptions regarding quark masses. In particular, the masses of the light ‘sea quarks’ are unrealistically heavy in order to make their contributions to the calculations tractable. This is known to be wrong, however, particularly for the u and d quarks, which are very light indeed. It was only with the development of fully unquenched QCD models that Lattice QCD has matured into a field which is capable of making predictions that are really interesting to test experimentally. The first fully unquenched calculation was for a very simple quantity, so as to start with the simplest first. It involved looking at what is known as the decay constant of the D^+ meson, or f_{D^+} . This can be thought of simply as the overlap of the wavefunctions of the two valence quarks

in the D^+ meson. If one were to think of them as being in a state roughly like a hydrogen atom, this is in some ways equivalent to the value of the wavefunction of the hydrogen atom at the origin. Obviously the interactions between the c and \bar{d} is immensely more complicated than that between the proton and electron, but the analogy between $\Psi(0)$ and f_{D^+} still holds.

Lattice QCD/Experiment (no free parameters!):

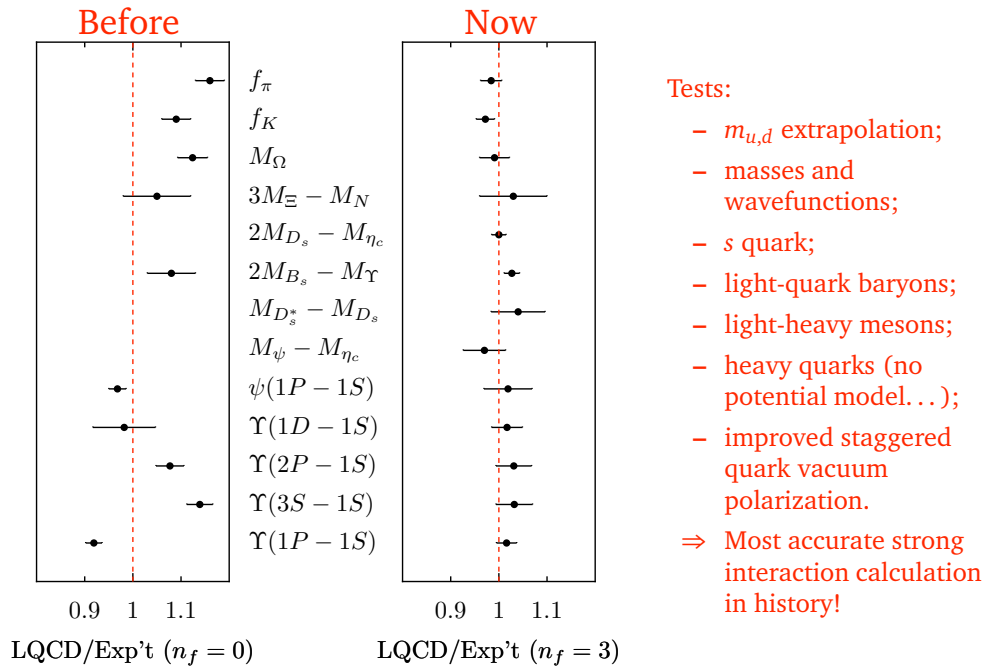


Figure 1.2: A series of predictions from unquenched lattice QCD, and their earlier counterparts (from [2]).

A number of the first unquenched lattice predictions are shown, with their earlier counterparts, in Figure 1.2, showing the tremendous improvement found, as well as their agreement with experiment. The first truly *predictive* calculation using an unquenched lattice model (i.e. of a quantity not previously measured experi-

mentally) was published in 2004 with a result of $f_{D^+} = 201 \pm 3_{\text{stat}} \pm 17_{\text{syst}}$ MeV [6]. The systematic uncertainty comes from a number of different sources, each of which contributes a small amount. This result was, however, published at the same time as the CLEO-c collaboration was able to publish the first reasonably precise measurement of f_{D^+} , which gave the result of $f_{D^+} = 221.6 \pm 16.7_{\text{stat}}^{+2.8}_{-3.4_{\text{syst}}}$ MeV [7]. The latter is clearly dominated by a lack of statistics, indicating that more data would be helpful in helping to give a more precise result, or that alternate analysis approaches might also be helpful in achieving this goal. It certainly seemed like it would be interesting to produce an experimental result more precise than the theoretical prediction. In the time since that first unquenched lattice calculation was published, the HPQCD collaboration has made tremendous strides in developing improvements to the technique. The most important of these is the development of what is known as the Highly Improved Staggered Quarks (HISQ) [8], which has carried with it major implications for the precision of these measurements.

What are staggered quarks, however? An undesirable side-effect of putting the Dirac equation on to a lattice is that, rather than solving for a single fermion, you end up solving for sixteen identical copies of this fermion. These are known as different ‘tastes’ of quark, to distinguish them from the real different flavors of quarks (since the different tastes are in no way physical). Staggering quarks is a way of reducing the number of ‘tastes’ of quarks from sixteen to four. Which seems like a good idea. The problem is that there are large discretization errors ($\mathcal{O}(a^2)$) associated with this technique, and it was only in the last ten years or so that people were able to deal with these (the goal being to suppress taste-exchange interactions, since those are clearly unphysical). At tree-level, these interactions can be suppressed or removed by smearing the gluon fields, and it was a thorough analysis of this which allowed the “ASQTAD” quark action to provide the result

mentioned from [6]. The HISQ approach is the first attempt to properly analyze and suppress the $\mathcal{O}(a^2)$ discretization errors completely at both tree-level and one-loop level, which it does remarkably well. An additional side effect of this new staggering technique is that it allows for charm quarks to be treated in the same way as light quarks; this had not previously been done. The net result of this is that it is now possible to drastically reduce the systematic uncertainties on predictions regarding the charm-quark system using calculations from LQCD. The most recent calculated value (from 2007), which uses the HISQ action yields $f_{D^+} = 207 \pm 4 \text{ MeV}$ [9], where the error is a combination of all systematic and statistical uncertainties. Having a 2% precision prediction to be aiming for provides all the more motivation for improving the experimental technique for measuring the leptonic decays of the D^+ meson.

1.3 The Simplest Decay

What does f_{D^+} have to do with leptonic decays of the D^+ , we may very well wonder. Everything, it turns out, as we shall shortly see. The decays of the D^+ are all weak decays, mediated by the W boson. The simplest possible decay will occur when the c and the \bar{d} annihilate to form a virtual W^+ , which then turns into a $\ell-\nu$ pair. The Feynmann diagram for this is shown in Figure 1.3. There are a number of reasons why this is such a simple decay process, but let us consider them in turn. The most important from the point of view of Lattice QCD is that it includes just two quarks. Unlike hadronic or even semi-leptonic decays, there are no other quarks polluting the mix, making things more complicated; there are only the two. Looking at the other side of things, there is only one thing coming out of the process on the other side: it's a two-body decay, making calculations

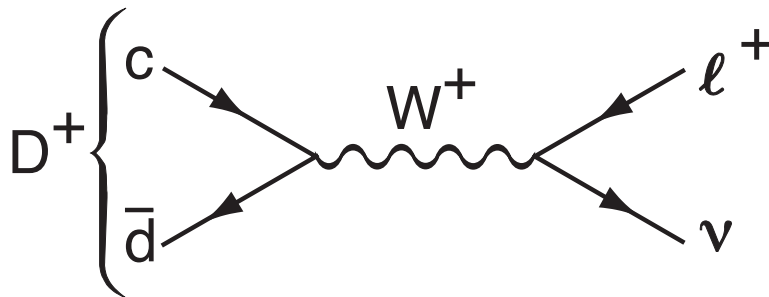


Figure 1.3: The Feynmann diagram for the purely leptonic decay of the D^+ meson.

of it considerably easier as well, as we shall shortly see. Let us consider how to calculate the matrix element for this transition from a more general perspective.

In general terms, we would write the interaction Lagrangian for a $V - A$ charged weak current operator \mathcal{J}^μ which couples to the W boson as

$$\mathcal{L}_{int} = -\frac{g}{\sqrt{2}} (\mathcal{J}^\mu W_\mu^+ + \mathcal{J}^{\mu\dagger} W_\mu^-) \quad (1.1)$$

where we have that

$$\mathcal{J}^\mu = \sum_{i,j} V_{ij} J_{ij}^\mu = \sum_{i,j} \bar{u}_i \gamma^\mu \frac{1}{2} (1 - \gamma_5) V_{ij} d_j \quad (1.2)$$

for quark currents. The indices i and j run over the three quark generations so that the field operators \bar{u}_i create u , c and t quarks, while d_j annihilates d , s and b quarks. V_{ij} is the CKM matrix element corresponding to mixing of the eigenstates. Analogous to this there is also a lepton current, but for it there is no mixing between generations (at least not at any level we are interested in); the ‘ L_{ij} ’ is therefore simply the unit matrix. We can write it in terms of Dirac spinors as

$$L^\mu = \bar{u}_\ell \gamma^\mu (1 - \gamma_5) v_\nu. \quad (1.3)$$

We will also use an approximate form for the W propagator and make use of the relation $G_F/\sqrt{2} = g^2/8M_W^2$ (which holds for processes in which the energy is much less than the W mass, as is most certainly the case here). This lets us write a general semi-leptonic decay matrix element as

$$\mathcal{M}(M_{Q\bar{q}} \rightarrow X_{q'\bar{q}}\ell^-\bar{\nu}) = -i\frac{G_F}{\sqrt{2}}V_{q'Q}L^\mu H_\mu \quad (1.4)$$

where H_μ is the hadronic current. In general this is a complicated matter since it involves the initial state quarks and the final state mesons, which make things rather difficult. Much effort is therefore put into the art of parameterizing these into *form factors*. However, for the purely leptonic decay, things are much simpler. There is only one possible choice of hadronic current to use: the quark current of the initial meson (shown in Figure 1.3) which will then just be the four-momentum of the D^+ meson q_μ (multiplied by some constant). This is then contracted with the leptonic current to give our answer.

$$\mathcal{M}(D_{c\bar{d}} \rightarrow \ell^+\nu) = i\frac{G_F}{\sqrt{2}}f_D V_{cd}L^\mu q_\mu \quad (1.5)$$

This *decay constant*, which is equivalent to a very simple form factor (simple in that it is constant and doesn't depend on any kinematic variable in the decay). Since this decay requires the quarks to annihilate, this form factor is, as previously mentioned, simply a measure of the overlap of their wave functions. It contains within it all of the QCD and internal interaction of the meson of this decay; everything else is simply kinematics.

The result of these kinematic factors is

$$\Gamma(D^+ \rightarrow \ell^+\nu) = \frac{G_F^2}{8\pi}|V_{cd}|^2 M_D m_\ell^2 f_D^2 \left(1 - \frac{m_\ell^2}{M_D^2}\right)^2 \quad (1.6)$$

where there are now a number of important additional factors worth mentioning. Firstly note the presence of m_ℓ^2 . This was actually present in the previous

expression as well (in the L^μ term), but now appears explicitly. This heavily suppresses the electronic decay, also suppresses the muonic decay relative to the τ decay. It is because the ℓ - ν system must be produced in an $L = 0$ state in order to conserve angular momentum (since the D^+ is spinless). This means that their spins must be anti-aligned; since the ν is purely left-handed, the ℓ must be formed in a mostly right-handed state. However, right-handed particles do not interact with a W boson, giving rise to the factor of m_ℓ^2 . Somewhat balancing out this factor is the pure phase space factor of $(1 - m_\ell^2/M_D^2)^2$. Because the τ mass is so close to the D mass, there is very little phase space in which the decay $D^+ \rightarrow \tau^+\nu_\tau$ can occur, even though the m_ℓ^2 factor would otherwise heavily favor it. As a result of this, the relative widths of the three leptonic decay channels are $2.65 : 1 : 2.3 \times 10^{-5}$ for $D^+ \rightarrow \tau^+\nu_\tau$, $D^+ \rightarrow \mu^+\nu_\mu$ and $D^+ \rightarrow e^+\nu_e$, respectively.¹ Since the muonic width is only slightly smaller than the tauonic, we will choose to measure the process $D^+ \rightarrow \mu^+\nu_\mu$. The τ lepton is not stable and decays quickly in the detector, producing events with multiple neutrinos (which we will see later are difficult to reconstruct), and it is therefore highly advantageous to study the much simpler mode $D^+ \rightarrow \mu^+\nu_\mu$. This is still not without difficulties, as we shall see, particularly since these leptonic decay widths are small. We also see a single factor of M_D ; one factor is lost to phase space [10, 11]

1.4 CLEO-c and f_{D^+}

CLEO-c has devoted a considerable amount of its running time to studying D mesons by collecting data at the $\psi(3770)$. The CLEO-c environment is particularly

¹This assumes that the standard model holds, of course. That is an assumption we will make for the purposes of this analysis.

well suited to the study of the the D mesons and to performing a measurement of f_{D^+} for a number of reasons. Firstly, the $\psi(3770)$ state decays exclusively to $D\bar{D}$ pairs², which gives a very clean sample. Secondly, the $D\bar{D}$ pairs are produced almost at threshold; they are therefore almost at rest in the lab frame with a momentum which is only on the order of a few hundred MeV/ c . Furthermore, CLEO-c is a symmetrical accelerator, so the two D mesons produced will have equal energies and equal and opposite momenta³.

The challenge of reconstructing $D^+ \rightarrow \mu^+ \nu_\mu$ is that neutrinos are by their nature essentially undetectable. Additionally, CLEO-c does not have a muon detector that is useful for particle identification at this energy. This means that we are essentially trying to reconstruct the decay of the D^+ into a particle which cannot be detected and a particle which cannot be well identified; clearly this is a challenge. Fortunately, there are ways of discriminating our signal from the many types of background, as we will see in Chapter 3.

²While there may be some very small exceptions to this, it is at the barely measurable level.

³These energies and momenta are in fact corrected slightly in order to account for the very small crossing angle of the beams.

Chapter 2

The CLEO-c Detector

2.1 Detector Overview

The CLEO-c detector is a highly hermetic detector consisting of a variety of different components designed to measure the products of electron-positron collisions created at the CESR-c (Cornell Electron Storage Ring) facility at Cornell University. The storage ring operates with symmetric beams, each at an energy of 1.5–2 GeV. This analysis uses a total of $281 \pm 2.8 \text{ pb}^{-1}$ of data taken at the $\psi(3770)$ resonance, corresponding to a beam energy of $E_{\text{beam}} \simeq 1.865 \text{ GeV}$. The detector is generally cylindrically symmetric, as is shown in the three-dimensional representation of the detector in Figure 2.1.

2.2 Drift Chambers

Tracking of charged particles is done using two concentric drift chambers, which are composed of thousands of wires strung from end to end of the chamber. The wires fall into two categories: sense wires and field wires. The sense wires are held at high voltage and the field wires are held at ground so as to keep a large electric field in the volume between the wires. The outermost electrons in the gas molecules (a helium-propane mixture) are only very loosely bound, and as such they can easily be stripped off by the passage of a high energy charged particle. When a particular electron is knocked loose, it feels the strong electric field and will accelerate towards the wire held at positive voltage. This will free other electrons,

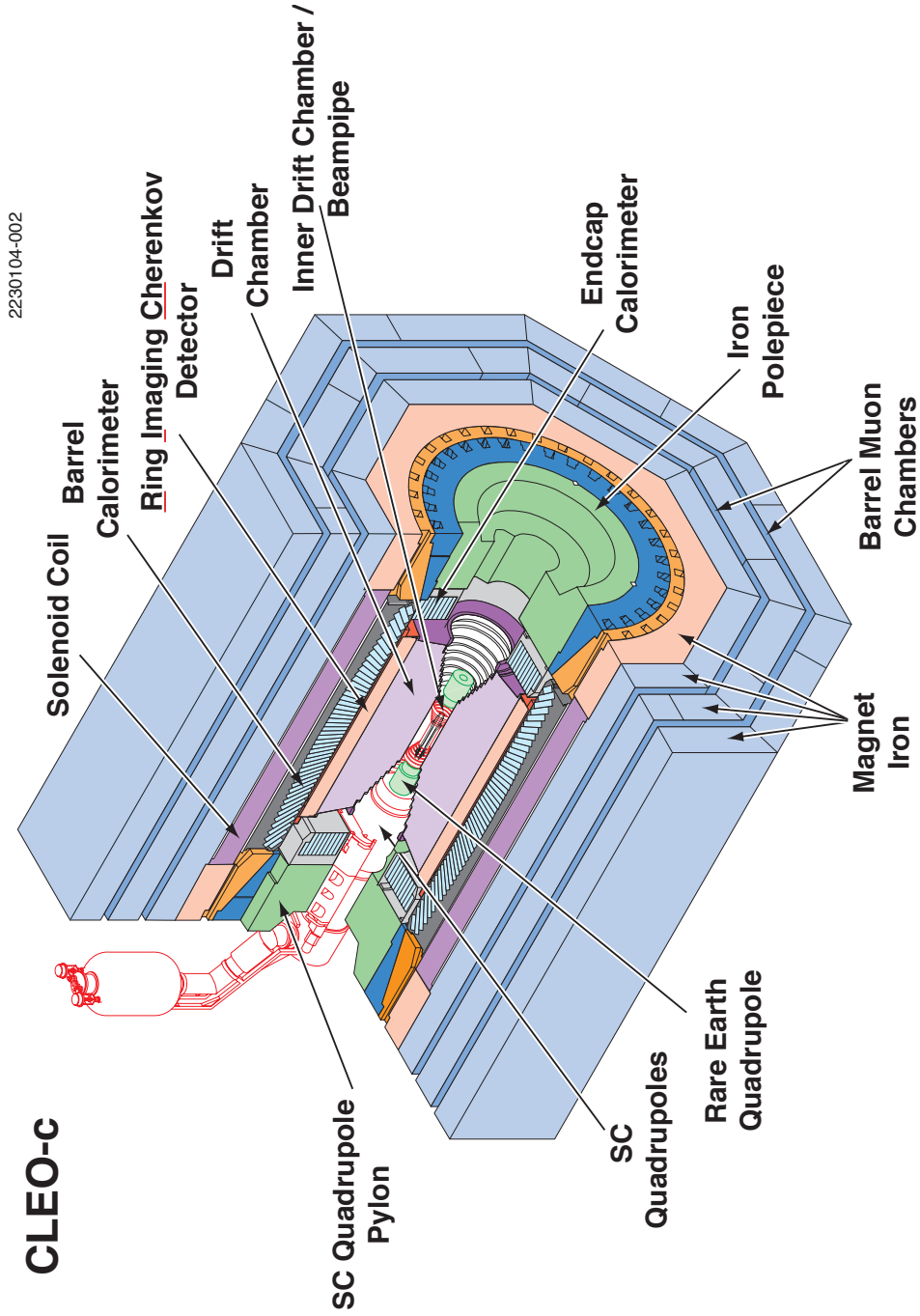


Figure 2.1: A cutaway view of the CLEO-c detector showing its chief components.

eventually creating a cascade of electrons which will be deposited on the wire. The typical gain created by this process depends strongly on the voltage of the wire with the gain doubling roughly every 50 V. [12]

As the particles move through the drift chamber, they lose energy, and the rate of this loss (or dE/dx , as it is known) depends on the mass and speed of the particle. This means that it is possible to use this information as one means of particle identification. [13]

2.2.1 Inner Stereo Drift Chamber: ZD

The innermost portion of the CLEO-c detector is a six layer drift chamber strung with a very high stereo angle (between 10.3° and 15.4°). It extends from the beam-pipe out to about 15 cm out. The stereo angle allows for tracking of particle in their z -momentum, even at very low r , which is useful for low momentum tracks. The voltage of the inner drift chamber is held at 1900 V, somewhat lower than the rest of the drift chamber because of the smaller size of the drift cell, and because, although it has a lower gain than the rest of the drift chamber, it reduces the danger of radiation damage to the ZD. Because of its close proximity to the beam, there was more chance of damage because of prolonged exposure from beam spray causing a buildup of ions on the wires than is the case for the DR.

2.2.2 Main Drift Chamber: DR

The main drift chamber is a forty-seven layer wire chamber held at 2100 V. It is composed of an inner, axial, portion, and an outer, stereo, portion. The innermost

sixteen layers are axial in nature, meaning that they are strung straight from end to end without any stereo angle. This makes them useless in determining the z -positional information of the track. However, they still provide x and y information, and this part of the drift chamber is particularly important for the triggering system, which uses the axial wires in a very simple way to trigger on simple track recognition algorithms in order to determine whether or not an event is worth recording or not. Track recognition in the outer layers is not as simple because of the stereo angle (and it is partly for this reason that the ZD is not used in triggering), although there are triggers that make use of outer tracking chamber layers for triggering. The outer thirty-one layers of the DR are stereo in nature and provide excellent resolution in terms of x , y , and z positions of the tracks. In groups of four layers at a time, they are strung in alternating positive and negative directions of stereo angle so as to give a stereoscopic view in terms of the z position of a wire.

It is not necessary to have all forty-seven layer hits in order to make a good helical fit to the track, so we generally have a highly over-constrained track because of our excellent tracking system. The combined effect of our drift chambers is to give us a momentum resolution on our tracks of approximately 0.6% at 800 MeV.

2.3 Ring Imaging Cherenkov Detector: RICH

The RICH is a crucial component for the CLEO-c because it provides a crucial level of particle identification above and beyond that given by the dE/dx information from the drift chamber. The basic principle of the RICH chamber is that when a particle is traveling through a medium at a speed faster than the speed of light in

that medium, it will give off radiation, called Cherenkov radiation, in the form of a cone of coherent light called. The half-angle θ_C of this cone is given by

$$\cos(\theta_C) = \frac{1}{n\beta} \quad (2.1)$$

where n is the refractive index of the material and β is the speed of the particle relative to the speed of light, i.e. $\beta = v/c$. By measuring the angle, we can measure the speed of the particle. Since we obtain a measurement of the momentum from the drift chamber, we can combine these to know the mass of the particle.

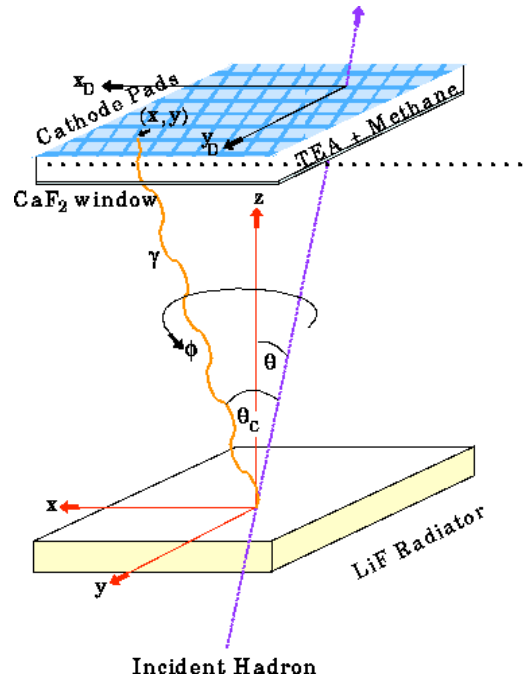


Figure 2.2: A schematic representation of the RICH detector in CLEO-c.

Figure 2.2 is a schematic representation of the RICH detector, showing an emitted photon as well as the incident charged particle's continued track. As is seen Figure 2.1 the RICH detector is located directly outside the drift chamber, with the LiF radiator being the material in which the Cherenkov photons are emitted. [14].

For CLEO-c we make use of hypotheses based on each of the different types of charged particles that we can have in the drift chamber (π , e , μ , K and p) and determine the Cherenkov angle that a given particle species will have as a function of momentum for all of the different points of the detector. A given particle's likelihood is then measured against each of these hypotheses, using all available photons in the RICH detector which fall within 5° of the expected Cherenkov ring for that species's particle hypothesis. One can then compare likelihoods for different particle hypotheses and uses this as a measure for determining particle identification.

It should be noted that the solid angle coverage of the RICH is considerably less than that of the rest of the detector; it covers only the region of $|\cos\theta| \leq 0.7$, whereas the drift chamber and calorimeter (discussed below) cover out to $|\cos\theta| \leq 0.93$. This is because there is no RICH coverage in the end caps, only in the barrel.

2.4 Electromagnetic Calorimeter: CC

The electromagnetic calorimeter is composed of 7784 CsI crystals (doped with a small amount of Th) each of which is 30 cm long and 5×5 cm on the ends. These crystals are arranged in two end cap sections and a barrel section, as shown in Figure 2.3. Note that the crystals in the barrel region are angled to point towards the interaction point so that photons will not strike the crystals from the side.¹

Because the crystals are very dense, high energy particles, and high energy photons in particular, will interact many times in the crystals. Every time the

¹The barrel crystals actually point slightly away from the interaction point so that photons do not slip between the crystals. This would be more likely to happen if they were all pointed directly at the interaction point.

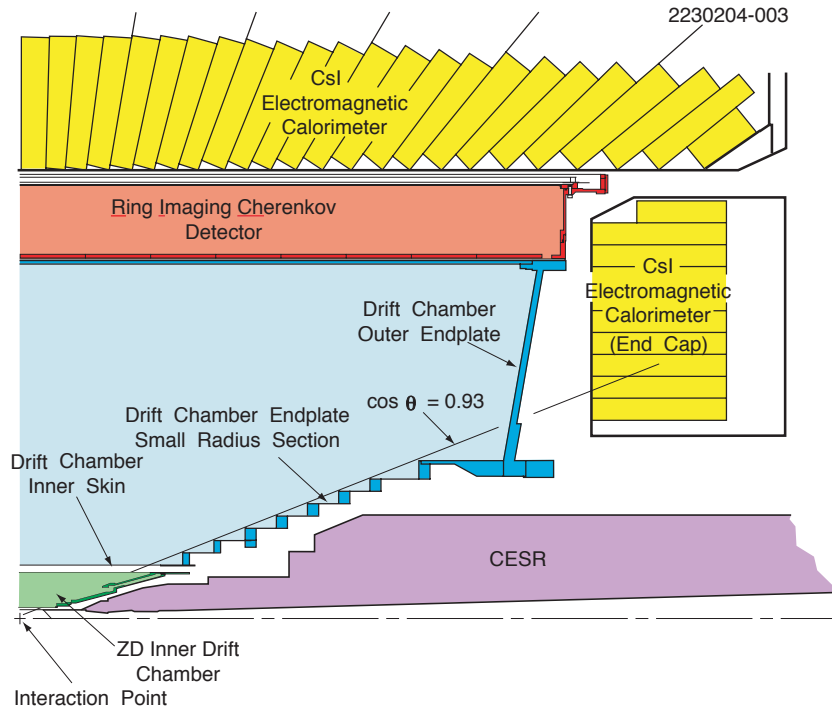


Figure 2.3: A side view of the CLEO detector, showing the angling of the CC crystals. This also shows the relative positioning of the ZD, DR, RICH and CC detectors.

γ rays do so, they convert their energy into a shower of daughter particles which eventually cause excitations of the atoms in the crystals which are measurable as optical light. Four photo-diodes on the back of each crystal measure the total deposited energy in a given crystal. A given particle will typically deposit its energy in a large number of neighboring crystals. Showers resulting from neutral particles are distinguished from those coming from charged particles in that their location does not match up to that of a charged track in the drift chamber; this allows for so-called track-shower matching, and the identification of showers that are matched to charged tracks.

Particles which interact chiefly through the electromagnetic interaction (e^\pm and γ) will deposit all of their energy in the calorimeter while other particles may well

only leave part of it there. In particular, μ will interact only slightly in the CC, leaving a small amount of energy (on the order of 200 MeV) regardless of the energy of the incoming particle. Hadronic particles, such as K and π will typically leave a more complicated shower structure than a μ but will not deposit all of their energy in the way that an electron will. This is used for identifying electrons in the CLEO-c electron ID package [15].

2.5 Muon Detectors

The outermost part of the CLEO-c detector is composed of the iron for the return yoke for the superconducting magnet and previously used to house the muon detection chambers. These were still operational for CLEO-c running, but the minimum energy required for a muon to punch through to these chambers was such that they were no longer useful for muon identification. A muon would need well over 1 GeV in order to reach these chambers, and since we are looking at decays where the typical energy level of particles is below 1 GeV, these chambers are not useful for any kind of particle ID. The muon chambers are useful for filtering out cosmic events, however, and are used in early stages of data processing for that purpose.

Chapter 3

Event Reconstruction

3.1 Overview

What we are trying to reconstruct is ultimately the decay of the $D^+ \rightarrow \mu^+ \nu_\mu$. Note that for simplicity, we will always refer to the signal D side as being the D^+ , although we obviously also consider the charge conjugate as well. This means that we will refer to the other side D as being a D^- , although if the signal side D is a D^- , it will obviously be a D^+ .

The technique we are using to measure this mode is called neutrino reconstruction. But what do we mean by the term *neutrino reconstruction*? In the context of this analysis, it is a technique whereby we essentially completely reconstruct the entire event using the best guess particle ID and track-shower matching in such a way as to count the total energy and momentum of the event. If the event has the signal side characteristics that are reasonably near what we are looking for (in our case this means a large amount of missing momentum and energy paired with a charged π^\pm candidate which make something resembling a reasonable D candidate, it is passed on for further consideration. The showers in particular are examined to see whether they are the products of hadronic decays (whether they match up to form π^0 's and η 's), and spurious extra showers are discarded. This gives a more precise measure of the energy of the other side D meson as well as a better measurement of the missing energy in the event overall.

For neutrino reconstruction analyses it is crucial to ensure that all momentum and energy in the event is measured correctly. In previous analyses this has been

done by simply using a combination of Trkman [16] for tracks and Splitoff [3] for showers. We use a multi-stage approach which can be termed an *improved neutrino reconstruction* technique, or a *hybrid neutrino reconstruction*, since it relies on essentially completely reconstructing all of the other side of the event; it is thus in some respects more like a universal tagging technique.

3.2 Trkman

Trkman is a software package developed specially for neutrino reconstruction whose purpose is to ensure the correct total counting of energy and momentum of charged particle tracks in events. The particular issue addressed by Trkman is when a charged particle creates multiple tracks in the drift chamber; Trkman chooses the track most likely to be the original track and discards the rest. This most commonly occurs with low-momentum tracks where the transverse momentum is sufficiently low that the track curls around inside the drift chamber; this is called a ‘curler’. The maximum transverse momentum for a particle to curl around in this manner is 250 MeV, corresponding to a radius of curvature of 0.82 m. It is also possible for higher momentum tracks to have curlers, however, if they splash back from an interaction in the calorimeter. The other ways in which bad tracks can arise is because of decays in flight (again giving multiple tracks where there should be one) or simply because the track is reconstructed in an area of very poor detector coverage. Trkman classifies all tracks according to codes with most (roughly 80%) being given the code 0, indicating that they do not need any processing. Tracks that are passed by Trkman are given positive codes while ones that are rejected by the algorithm are given negative codes. The two parts of a two-curler might thus be given the codes ‘201’ and ‘-201’, for the front and back halves, respectively.

Run: 202742
Event: 98595

1630804-076

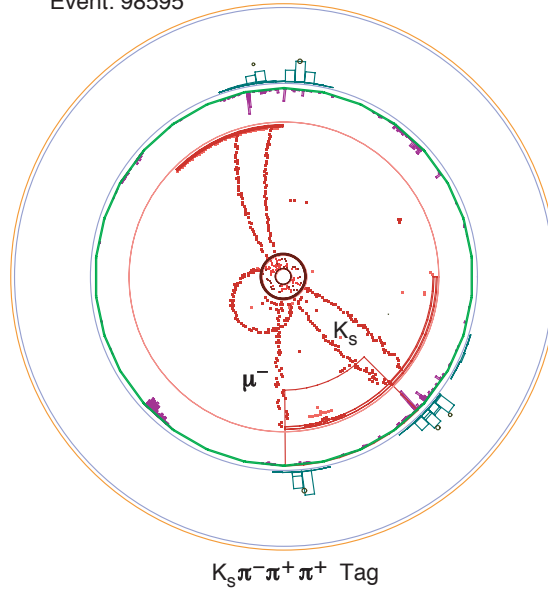


Figure 3.1: An event from data showing a $D^+ \rightarrow \mu^+ \nu_\mu$ event containing a curler.

Trkman looks at all tracks and groups them into two (and potentially three or more) curlers which are then analyzed. Different parameters of the tracks, such as hit density,¹ distance of closest approach to the interaction point in both z and r , and $\cos \theta$ are then analyzed and used to determine which of the two tracks is more likely to be the ‘front’ half, and which is more likely to be the back half. This was tuned using a large sample of Monte Carlo (MC) simulations. The approach from two-curlers is applied to three-curlers and beyond, although in this case Trkman must first pick the most likely ‘front-back’ pair and then use the algorithm on that pair.

In-flight decays of particles, hard scatters off material and other are also handled by Trkman. It identifies these tracks after having excluded curlers by looking for

¹Hit density means the number of hits on drift chamber wires divided by the number of expected hits on drift chamber wires.

other pairs of tracks and then determines which of the two is the ‘correct’ track using selection criteria based on the density of hits and closest approach to the beam.

Trkman also imposes some very basic track quality cuts on all tracks in order to remove the most spurious tracks. Tracks with a fitted momentum of over 6.5 GeV are discarded, as are tracks with zero curvature. Furthermore, tracks with a hit density of less than 0.5 are discarded, as are tracks with a hit density of less than 0.6 and a distance of closest approach to the beam of greater than 1 cm. [16]

3.3 Splitoff

Where Trkman is an attempt to avoid double-counting the energy and momentum of tracks in the drift chamber, Splitoff is an analogous attempt to do the same with the energy of showers in the calorimeter. The problem arises in counting up the total energy of an event. Counting up the total energy of the tracks is simple (provided one can identify the particles), but one must then add in all the neutral energy as well. If one were to simply add in all the energy in the calorimeter, one would be double-counting all of the energy deposited in the calorimeter by the charged particles. Dealing with this is a multi-stage process, which we will go over in detail below.

The first step is the simplest to perform, and involves ‘track-shower matching’, in which we match up tracks in the drift chamber with corresponding showers in the CC towards which they geometrically point. These showers can then be eliminated from the list of showers for determining the energy of the event (and for identifying potential π^0 ’s, for instance), since they are from charged particles,

not γ 's.

Leptons typically deposit all of their energy in a small volume of crystals, either because they are minimum ionizing (in the case of μ^\pm) or because they interact abruptly with the CsI (in the case of e^\pm). In either case, they will tend to leave only a single shower associated with their interaction with the calorimeter. This is unfortunately not the case with hadrons. Both π^\pm and K^\pm will tend to interact with the crystals in such a way as to create splashes in the calorimeter, so that their showers are larger geometrically and also more likely to contain ‘split-offs’, where a smaller shower nearby will be distinct (geometrically) from the main shower.

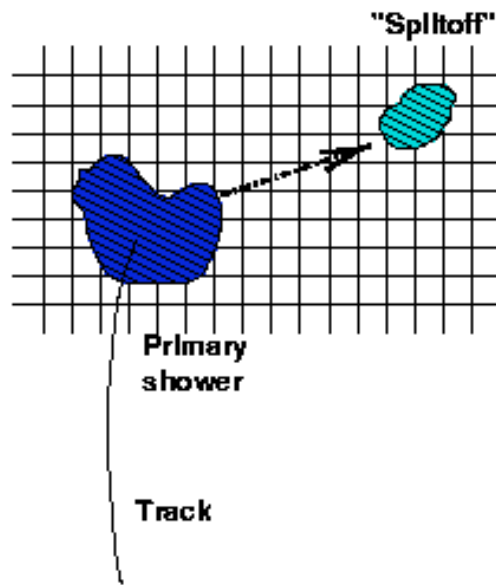


Figure 3.2: An representation of a split-off. The image is from [3]

Splitoff uses a neural network algorithm to identify these showers and remove them from the list of ‘real’ showers so that their energy is not added, incorrectly, to the energy of the event. This has been a standard part of neutrino reconstruction analyses for the past decade, and although the technique has been tuned somewhat

(to adapt to the lower energy environment of CLEO-c), the basic approach remains the same. [3]

3.4 Initial Neutrino Reconstruction

The simple neutrino reconstruction package sums the energy and momenta of all the Trkman approved tracks and Splitoff approved showers in the event. The energy of a track is determined using a particle ID package which combines the RICH and dE/dx information (if no RICH information is present, only dE/dx is used) into a combined log-likelihood for different particle hypotheses; the most likely particle variety is then chosen. The standard CLEO electron ID package is used to identify electrons [15] and events containing electrons are vetoed.

Having determined which tracks are to be included, the total energy and momentum in the tracks is then easy to calculate:

$$\vec{p}_{\text{tracks}} = \sum_{\text{tracks } i} \vec{p}_i \quad (3.1)$$

$$E_{\text{tracks}} = \sum_{\text{tracks } i} \sqrt{(\vec{p}_i^2 + m_i^2)}. \quad (3.2)$$

where the sum runs over all Trkman-approved tracks in both cases. For the showers, the classic neutrino reconstruction takes all the Splitoff approved showers to be the result of photons and adds their momenta and energies. Note that showers matching up with tracks have already been filtered out by Trkman and track-shower matching. We take

$$\vec{p}_{\text{showers}} = \sum_{\text{showers } j} E_j \hat{p}_j \quad (3.3)$$

$$E_{\text{showers}} = \sum_{\text{showers } j} E_j \quad (3.4)$$

where \hat{p}_j is a unit vector pointing in the direction of the shower.

The net four-momentum of the beams is well known from the beam energy and the crossing angle of the beams. Given the total observed and initial four-momentum, we can reconstruct the missing four-momentum in the event by simply subtracting the observed four-momentum from the center of mass four-momentum. This is the four-momentum of the reconstructed candidate neutrino:

$$E_{\text{miss}} = 2E_{\text{beam}} - E_{\text{tracks}} - E_{\text{showers}} \quad (3.5)$$

$$\vec{p}_{\text{miss}} = \vec{p}_{\text{CoM}} - \vec{p}_{\text{tracks}} - \vec{p}_{\text{showers}} \quad (3.6)$$

where \vec{p}_{tracks} , E_{tracks} , \vec{p}_{showers} and E_{showers} are defined in Equations 3.1, 3.2, 3.3 and 3.4, respectively. For a properly reconstructed event containing only one neutrino, the invariant mass of this four-momentum, as defined by

$$m_\nu^2 = E_{\text{miss}}^2 - |\vec{p}_{\text{miss}}|^2 \quad (3.7)$$

is going to be zero, since the invariant mass of a ν is zero. This will be one method we use to discriminate between our signal and various backgrounds; backgrounds will not in general tend to reconstruct cleanly with the hypothesis of one neutrino, and there will thus be no peak at zero event missing mass squared.

Our initial selection criteria for the event are that we have a large amount of missing momentum, greater than 650 MeV reconstructed, along with a good μ^+ candidate which together make up a candidate D^+ . At this point we now have a candidate event with a candidate D^+ , made up of a ν and a μ^+ , along with a candidate D^- , made up of everything else. There are certain properties of it that are examined even at this stage in order to determine whether or not it is a viable candidate to examine further.

3.4.1 ΔE

We note that the e^+ and e^- beams each contain an energy $E_{\text{beam}} = 1/2 \times 3.773 \text{ GeV}$. Because of this symmetry, both the reconstructed D^+ and D^- mesons must each have exactly this same energy. We will for now just use this requirement on the signal side and create the variable

$$\Delta E_{s.s.} = E_{\mu}^* + E_{\text{miss}}^* - E_{\text{beam}} \quad (3.8)$$

$$= E_{\mu}^* + |\vec{p}_{\text{miss}}^*| - E_{\text{beam}}. \quad (3.9)$$

We call it ΔE because it should be zero for a well reconstructed event, and has the subscript *s.s.* to denote that it relates to the signal side D . This relation properly holds only in the center of mass frame, and as such we transform the energy of the μ^+ and the ν candidate into that frame for this calculation, which is what the asterisk denotes. In Equation 3.9 we have made the substitution that $E_{\text{miss}} = |\vec{p}_{\text{miss}}|$ in order to improve our resolution. This is a reasonable substitution to make because, for our signal, it is correct, and we have a better resolution in our drift chamber (and thus in our momentum measurement) than we do in our calorimeter. Furthermore, errors in energy measurements tend to add (on average) whereas measurements in momentum tend to cancel out (on average), because momentum is a vector, whereas energy is a scalar.

For now we are making only the very loosest requirements, and requiring that $|\Delta E_{s.s.}| < 0.5 \text{ GeV}$. Figure 3.3 shows that this doesn't touch any signal in any way.

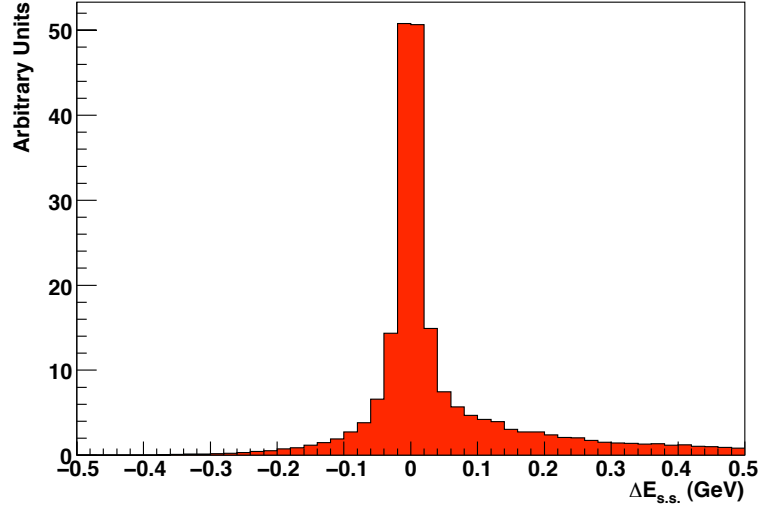


Figure 3.3: The $\Delta E_{s.s.}$ distribution for signal Monte Carlo (MC) events before any cuts are made.

3.4.2 M_{BC}

We write the *beam constrained mass* M_{BC} as

$$M_{BC} = \sqrt{E_{\text{beam}}^2 - (\vec{p}_\mu + \vec{p}_\nu)^2}. \quad (3.10)$$

It is not to be confused with the unconstrained mass of the $\mu - \nu$ system, or the D^+ mass:

$$M_{\mu-\nu} = \sqrt{(E_\mu + E_{\text{miss}})^2 - (\vec{p}_\mu + \vec{p}_\nu)^2} \quad (3.11)$$

$$= \sqrt{(E_\mu + |\vec{p}_{\text{miss}}|)^2 - (\vec{p}_\mu + \vec{p}_\nu)^2}. \quad (3.12)$$

Equation 3.10 and equations 3.11 and 3.12 are the same but for the substitution of the beam energy for the combined energy of the ν and μ in the case of 3.10. In both cases, for a perfectly reconstructed signal event, they yield $M_D = 1869.3$ MeV. However, the M_{BC} value is much less sensitive to mismeasurements in energy than is the measurement of $M_{\mu-\nu}$, and it will therefore be a much narrower distribution,

which is why we choose to use it as our variable in which to fit the data, ultimately and why we use it for our selection requirement now. For the present, we are simply interested in whether our events make up anything remotely like a good D^+ candidate, and we therefore veto events for which $M_{BC} < 1.75 \text{ GeV}/c^2$. These requirements are what are referred to as the very loose criteria in our figures. (see Figure 3.15 to see why this cut is still quite loose compared to the signal distribution)

3.5 Improved Neutrino Reconstruction

Having made these basic requirements, we now use an improved technique in order to try to deal with the extra showers which may be contaminating the event; this will give us a better resolution of the missing energy and of the energy of the D^- . In some sense, this can be seen as an extension of the Splitoff process in that we are attempting to ensure that the total energy of the event is calculated correctly by eliminating spurious showers in the calorimeter. Rather than simply trying to eliminate showers that are geometrically near a hadronic track, we are instead going to use a process of elimination to match up all the showers in the event in order to ensure that all the showers we use come from an actual physical decay process.

The assumption of the improved neutrino reconstruction technique is that essentially all *real* showers are from photons which are decay products of hadronic particles, either π^0 's or η 's. Radiative processes involving single photons are suppressed on the order of α and are therefore a very small contribution. Rather than treat the showers in the calorimeter which are not matched to tracks as coming

from individual photons, it would therefore make sense to try to pair them up with each other in order to try to reconstruct the π^0 and η particles.

The way in which we do this is as follows, in which all Splitoff-approved showers (which must also therefore be unmatched with Trkman-approved tracks) are used to try to form π^0 candidates using all combinations. We will now attempt to eliminate the showers using a simple algorithm. The best π^0 candidate is selected of all those present, defined as the one whose pull mass² is closest to zero. The showers associated with that π^0 are removed along with all other π^0 candidates which included those showers. The list is then re-examined and the best remaining π^0 candidate is removed, following the same procedure. This is repeated until there are no remaining π^0 candidates whose pull mass falls between -5.0 and 3.0 . This is the first stage. This will include most well reconstructed π^0 's, as is shown in Figure 3.4, which shows the pull mass distribution for ‘true’ (as defined by the Monte Carlo truth table) π^0 's, taken from signal Monte Carlo.

We now want to include less well reconstructed π^0 candidates, as well as potential $\eta \rightarrow \gamma\gamma$ candidates. The mass resolution of $\eta \rightarrow \gamma\gamma$ is not as good as that of π^0 as shown in Figures 3.5 and 3.6, which is why we consider $\eta \rightarrow \gamma\gamma$ pairs of photons only at this stage. They are allowed to be in the pull mass range of -15.0 to 15.0 , while we consider π^0 candidates in a slightly wider range: from -25.0 and 15.0 . If two showers A and B form both a π^0 and an η candidate, they will be matched to whichever candidate has the pull mass closer to zero. Remember, however, that the best π^0 candidates have already been taken away in the step above, so the likelihood of something forming a very good π^0 candidate is not great; also, the masses of the π^0 and the η are not close to each other (134.98 MeV

²The pull mass is defined as the difference between the expected mass and the measured mass, divided by the expected uncertainty. This uncertainty is typically obtained from Monte Carlo.

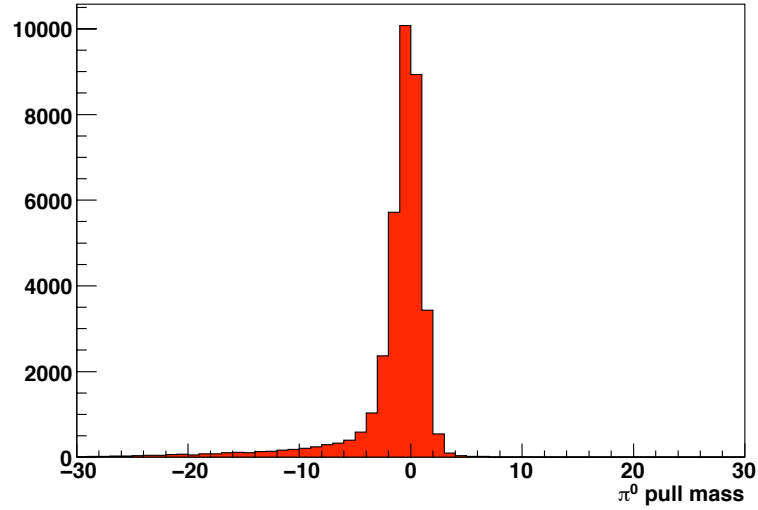


Figure 3.4: The pull mass distribution for Monte Carlo truth π^0 's.

and 547.51 MeV, respectively [13]).

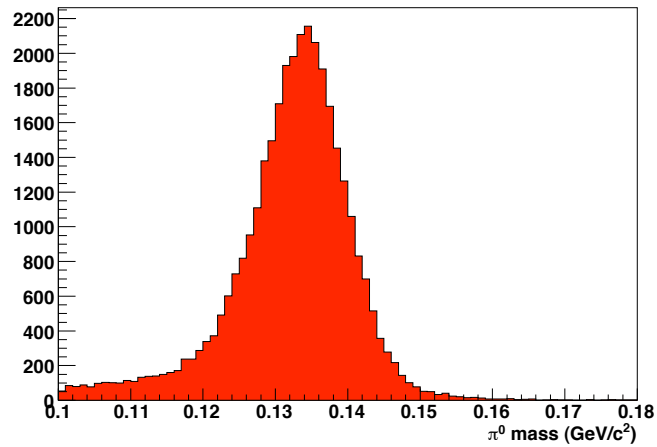


Figure 3.5: Mass resolution of MC truth π^0 's

At this point we veto any remaining showers with energies of less than 250 MeV under the assumption that they are most likely the product of a hadronic split off or noise. Vetoed showers' energies are not included in the calculation of the total energy of the event, nor are their momenta used to calculate the direction and

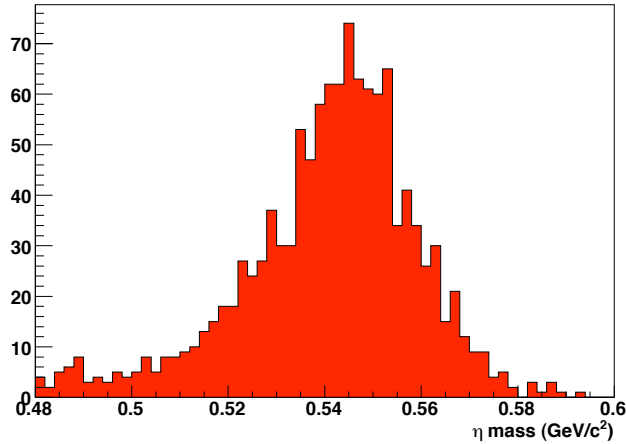


Figure 3.6: Mass resolution of MC truth $\eta \rightarrow \gamma\gamma$'s

magnitude of the missing momentum in the event. There may be some remaining showers that have been neither vetoed nor assigned to a π^0 or η . These are left in as photons.

The improved neutrino reconstruction does not have as great an effect on the missing momentum measurement for the event because the extra showers in the event will on average tend to cancel each other out (as mentioned above). However, it leads to a greatly improved missing energy measurement. Figure 3.7 shows the difference between the energy of the other side D -meson and the beam energy (this variable, called $\Delta E_{o.s.}$, is described in detail below) for events reconstructed using classic and improved neutrino reconstruction looking at signal Monte Carlo for $D^+ \rightarrow \mu^+ \nu_\mu$. The enhancement at zero is quite large and provides us with a selection criterion on which we will be able to make a much tighter cut than we otherwise would.

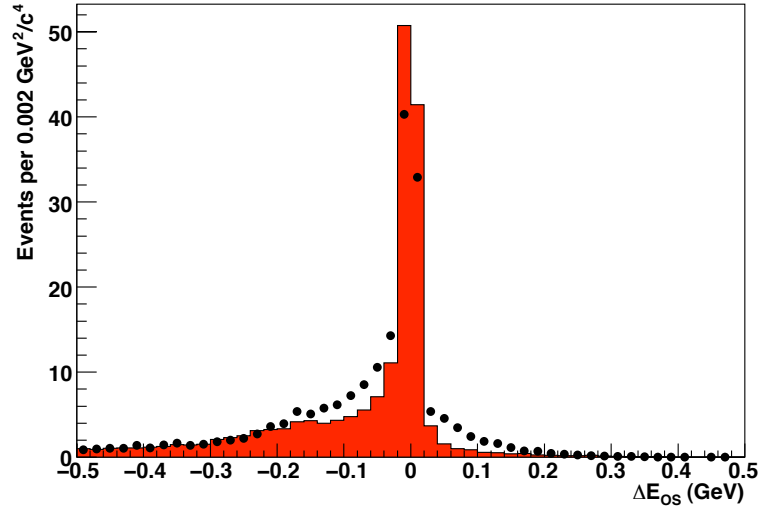


Figure 3.7: $\Delta E_{0.s.}$ for signal Monte Carlo without (black points) and with (solid red histogram) the improved other side shower reconstruction.

3.6 μ^+ Candidate Properties

We now consider the various further selection requirements we make on event and its various properties, starting with the μ^+ candidate. It must pass the following cuts:

- The distance of closest approach to the interaction vertex in the $x - y$ plane $|d_0| \leq 0.005$ m
- The distance of closest approach to the interaction vertex perpendicular to the $x - y$ plane $|z_0| \leq 0.05$ m
- The track has a $\chi^2 < 1000$ and a hit fraction > 0.3
- There is valid dE/dx information for the track
- The track must not be identified as an electron according to the standard

electron ID

- If there is valid RICH information for the track (which is the case the majority of the time) we require that there be at least three photons available for the RICH pion hypothesis. In this case the particle log-likelihood difference between a π and a K must be less than -10
- The energy deposited in the calorimeter in the shower matched to the track must be less than 285 GeV

The first four of these are simply to prevent poorly reconstructed tracks from being included. The last three are particle ID requirements to eliminate e^+ , K^+ and π^+ , respectively. Misidentified e^+ and K^+ make up an insignificant amount of background, but it is very difficult to remove π^+ backgrounds simply by applying standard particle ID requirements. Because of their very similar mass, it is impossible to use dE/dx or RICH information to distinguish between π^+ and μ^+ particles. The one selection criterion which is possible, is that the energy deposited in the CC must be that of minimum ionization. We therefore require that the energy deposited in the CC be less than 275 MeV. Plots of μ^+ and π^+ energy deposition in the calorimeter are shown in Figures 3.8 and 3.9, respectively. While the π^+ distribution also has a strong peak at 200 MeV, there is also a very long tail which can be eliminated with our criterion.

As previously mentioned, a given μ^+ candidate is of course paired with a ν candidate to form a D^+ , and the other tracks and showers (now π^0 's and η 's) form a D^- . We have already considered some of the properties of the event: m_{ν}^2 , $\Delta E_{s.s.}$, and M_{BC} . Let us consider these and others in more detail now.

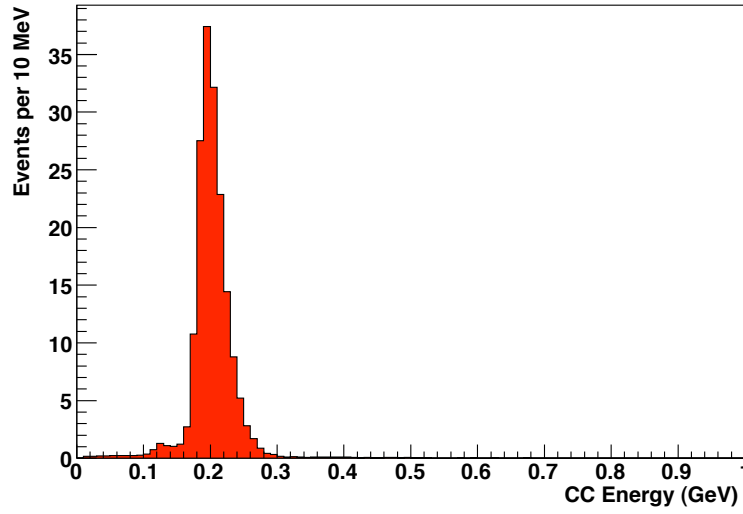


Figure 3.8: Energy deposited in the calorimeter by the μ^+ candidate track for signal Monte Carlo.

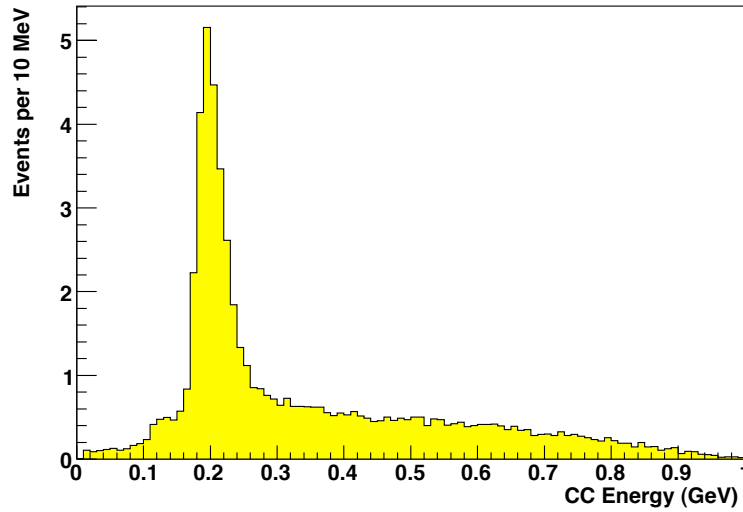


Figure 3.9: Energy deposited in the calorimeter by the μ^+ candidate track for $D^+ \rightarrow \pi^+\pi^0$ Monte Carlo where the μ^+ candidate is in fact a π^+ .

3.7 $\Delta E_{o.s.}$

We defined the $\Delta E_{s.s.}$ in Equation 3.9. We can make the same argument regarding the energy of the D^- as we did for the D^+ and thus define a variable for the other side energy:

$$\Delta E_{o.s.} = E_{\text{tracks}}^* + E_{\pi^0 s}^* + E_{\eta' s}^* + E_{\text{showers}}^* - E_{\text{beam}}, \quad (3.13)$$

The asterisk once again indicates that the energies should be evaluated in the center of mass frame. This is the variable whose resolution is most improved by the addition of the improved neutrino reconstruction, since we have eliminated spurious showers which degraded the quality of the signal. Like $\Delta E_{s.s.}$, $\Delta E_{o.s.} = 0$ for a well reconstructed event (the *o.s.* subscript denoting that it pertains to the other side D), but whereas $\Delta E_{s.s.}$ measures how well we reconstructed our D^+ candidate, $\Delta E_{o.s.}$ measures how well we reconstructed what was on the other side. These two variables need not be entirely correlated: it is possible to have a perfectly well reconstructed D^- and yet have a poor D^+ candidate. $\Delta E_{o.s.}$ is an excellent way of reducing backgrounds which do not come from true D decays and general combinatoric backgrounds. We use the range $-0.06 \text{ GeV} < \Delta E_{o.s.} < 0.05 \text{ GeV}$ to define our signal region (see Figure 3.10).

3.8 $MM_{s.s.}^2$

It turns out that there is a better variable to use than $\Delta E_{s.s.}$ for determining the quality of the reconstructed D^+ . The variable we choose to use is equivalent to what the existing tagged analysis ([7]) called the missing mass squared, or MM^2 . However, in order to avoid confusing this quantity with the event missing mass

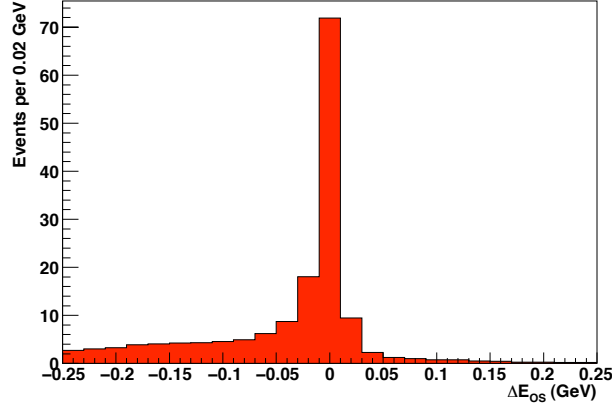


Figure 3.10: $\Delta E_{\text{o.s.}}$ for signal Monte Carlo with loose selection requirements. The tail on the left is dominated by lost showers.

squared m_ν^2 , we will call this variable the *signal side missing mass squared* or $MM_{\text{s.s.}}^2$. It is effectively a way of calculating the invariant mass squared of the ν , using constraints of the beam energy and the reconstructed μ^+ . We express it as

$$\begin{aligned}
 MM_{\text{s.s.}}^2 &= E_{\text{miss}}^2 - |\vec{p}_{\text{miss}}|^2 \\
 &= (E_{\text{beam}} - E_\mu)^2 - |\vec{p}_{\text{miss}}|^2,
 \end{aligned}
 \tag{3.14}$$

where we use the constraint from equation 3.8 that $\Delta E_{\text{s.s.}} = 0$, such that

$$E_{\text{miss}} = E_{\text{beam}} - E_\mu.
 \tag{3.15}$$

This is not a particularly large assumption to make. We are simply stating that the event is well reconstructed and that all of the missing energy comes from one missing particle in the event, i.e., that we have a well reconstructed ν candidate. If that assumption were false, we would tend to have a flat background since no particular value of $MM_{\text{s.s.}}^2$ will be favored. There are, however, a number of background components which will peak strongly in the variable $MM_{\text{s.s.}}^2$ at a

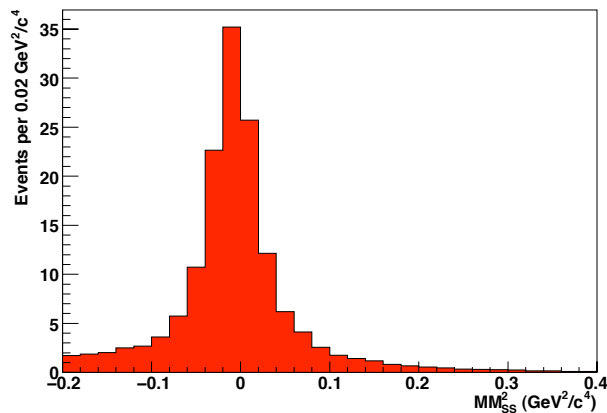


Figure 3.11: $MM_{s.s.}^2$ for signal Monte Carlo (with only loose selection criteria). The tails of the distribution are from cases where the event is not reconstructed properly because of additional neutrinos, K_L 's or lost showers.

value other than zero, precisely because they come from real decays of D mesons but contain other particles than neutrinos as their candidate. In particular, any background containing a K_L rather than a ν will have a $MM_{s.s.}^2$ value near $m_{K^0}^2$, rather than at zero. Looking at $MM_{s.s.}^2$ rather than $\Delta E_{s.s.}$ causes these backgrounds to peak at a physically meaningful value ($m_{K^0}^2 = 0.248 \text{ GeV}^2$). An example of this is shown in Figures 3.12 and 3.13 for the background $D^+ \rightarrow \pi^+ K_L$ (discussed in section 5.5.1).

Overall, $MM_{s.s.}^2$ gives a better discrimination between signal and background than making a cut based on $\Delta E_{s.s.}$, resulting in an improvement of the figure of merit on the order of one (see section 3.11). The requirement chosen is that events fall within the range $-0.08 \text{ GeV}^2/c^4 < MM_{s.s.}^2 < 0.08 \text{ GeV}^2/c^4$ in order to be included in the final sample.

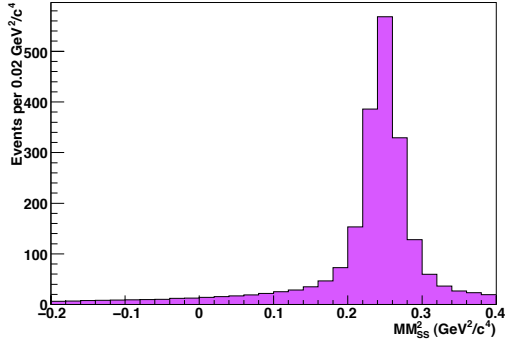


Figure 3.12: $MM_{s,s}^2$ for $D^+ \rightarrow \pi^+ K_L$

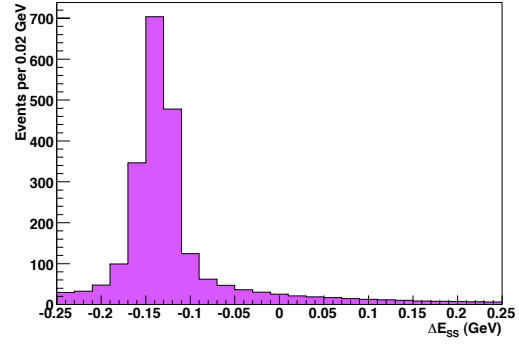


Figure 3.13: $\Delta E_{s,s}$ for $D^+ \rightarrow \pi^+ K_L$

3.9 m_ν^2

The missing mass squared of the event, or the mass squared of the neutrino candidate for the event, m_ν^2 , unconstrained by any beam energy, has already been mentioned above, as it is a key value to measure in classic neutrino reconstruction. It is also used in the improved neutrino reconstruction, at which point we have better measurements of E_{miss} and \vec{p}_{miss} , i.e.

$$E_{\text{miss}} = 2E_{\text{beam}} - \sum_{\text{tracks } i} E_i - \sum_{\pi^0_s j} E_j - \sum_{\eta_s k} E_k - \sum_{\text{showers } l} E_l \quad (3.16)$$

$$\vec{p}_{\text{miss}} = \vec{p}_{\text{CoM}} - \sum_{\text{tracks } i} \vec{p}_i - \sum_{\pi^0_s j} \vec{p}_j - \sum_{\eta_s k} \vec{p}_k - \sum_{\text{showers } l} \vec{p}_l. \quad (3.17)$$

We can now calculate m_ν^2 using these quantities as

$$m_\nu^2 = \left(2E_{\text{beam}} - \sum_{\text{tracks } i} E_i - \sum_{\pi^0_s j} E_j - \sum_{\eta_s k} E_k - \sum_{\text{showers } l} E_l \right)^2 - \left(\vec{p}_{\text{CoM}} - \sum_{\text{tracks } i} \vec{p}_i - \sum_{\pi^0_s j} \vec{p}_j - \sum_{\eta_s k} \vec{p}_k - \sum_{\text{showers } l} \vec{p}_l \right)^2 \quad (3.18)$$

For our final event selection we require events to fall within the range $-0.12 \text{ GeV}^2/c^4 < m_\nu^2 < 0.08 \text{ GeV}^2/c^4$. Note that this is a slightly wider win-

dow than that of $MM_{\text{s.s.}}^2$: this is because this variable is not constrained by the beam energy in the same way.

3.10 Other Criteria

One general problem that we need to address is what happens if there are charged particles that are never detected by the tracking chamber at all. If the direction of the missing momentum is pointing too close to the beam axis, the reason is most likely that there was simply a track or shower that was never reconstructed. We therefore ignore events for which the direction of the missing momentum is too close to the direction of the beam pipe. In order to reduce the large continuum background, we actually eliminate most of the end-cap region as well, and allow only events where

$$\cos \theta(\vec{p}_{\text{miss}}) \leq 0.81. \quad (3.19)$$

It is still possible that tracks could fail to be reconstructed, however, even in the main part of the drift chamber. If that were to happen, we would not want such a track to be mistaken for our candidate ν . In order to eliminate such misreconstructed events we therefore veto events for which the net charge of all included tracks does not add up to zero; the chance of two such tracks (of opposite sign) both failing to be reconstructed in precisely such a way so as to create a ν candidate is vanishingly small. We can write this as

$$\sum_{\text{tracks}} q_i = 0 \quad (3.20)$$

where q_i is the charge of the i th track and the sum is over all Trkman-approved tracks.

We also include a veto on events from the improved shower reconstruction: if they had more than 300 MeV of showers vetoed in them, we exclude the event. The assumption is that there must have been something very wrong with the event in order for that many showers to have been vetoed, and this happens very rarely in any case, as is shown in Figure 3.14. Another veto used for events was that if there is a single charged K identified in reconstructing the D^- , it must be a K^+ . We are assuming that we do not have a doubly Cabibbo-suppressed decay of the D^- , of course, but that is highly unlikely. This allows us to further reduce combinatoric backgrounds where particles have been swapped between the two D mesons. If there are both a K^+ and a K^- as part of the D^- , the accompanying π must be a π^- because of charge conservation.

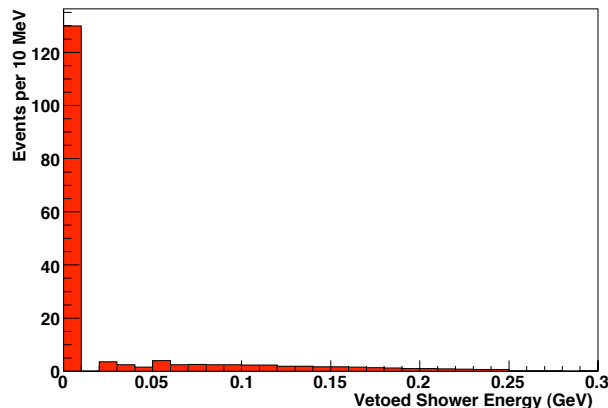


Figure 3.14: Total vetoed shower energy for signal Monte Carlo (with only loose selection criteria). Note that the majority of events have only a very small vetoed energy—nowhere near our cutoff of 300 MeV.

Table 3.1: Event Selection Criteria

<i>Selection Criterion</i>	<i>Requirement</i>
μ^+ track quality	$ d_0 < 0.005$ m, $ z_0 < 0.05$ m, hit fraction > 0.3 , $\chi^2 < 1000$
μ^+ CC shower	$E_{\text{shower}} < 285$ MeV
Direction of \vec{p}_{miss}	$ \cos \theta(\vec{p}_{\text{miss}}) < 0.81$
Net charge of event	$\sum_{\text{tracks}} q_i = 0$
m_ν^2	$-0.12 \text{ GeV}^2/c^4 < m_\nu^2 < 0.08 \text{ GeV}^2/c^4$
$MM_{\text{s.s.}}^2$	$-0.08 \text{ GeV}^2/c^4 < m_\nu^2 < 0.08 \text{ GeV}^2/c^4$
$\Delta E_{\text{o.s.}}$	$-0.06 \text{ GeV} < \Delta E_{\text{o.s.}} < 0.05 \text{ GeV}$
K^\pm veto	other side K^\pm must be same sign as μ^\pm
Vetoed Showers	Total vetoed shower energy < 300 MeV

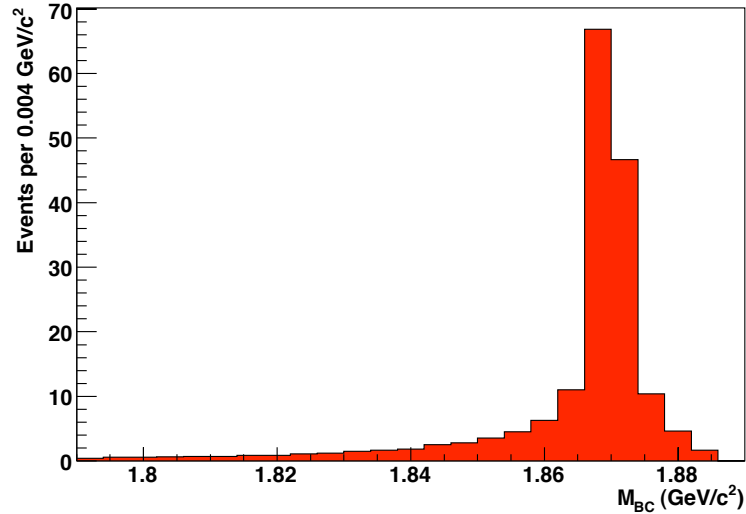


Figure 3.15: M_{BC} for signal Monte Carlo with only very loose cuts. The tails are caused by poor ν reconstruction.

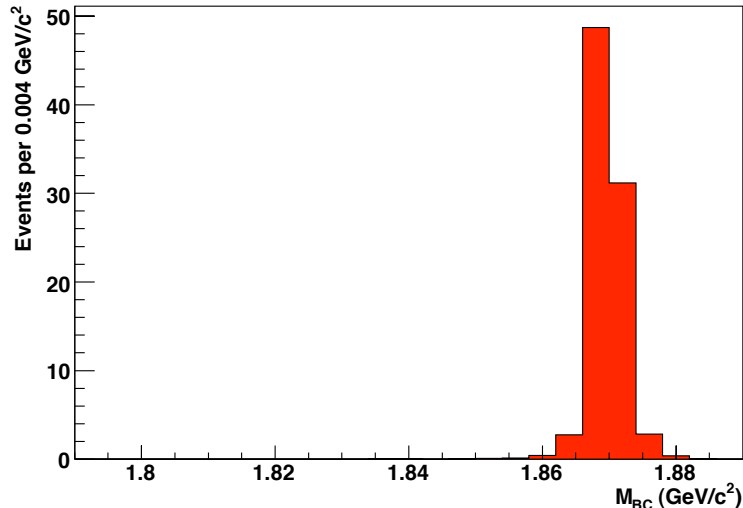


Figure 3.16: M_{BC} for signal Monte Carlo after all selection cuts.

3.11 Summary of Selection Criteria

For the sake of reference, we will here summarize the different selection criteria in Table 3.1. The values found for the event selection criteria were found using a tuning Monte Carlo sample of signal and background (different from the fitting sample) using an optimization algorithm designed to maximize the figure of merit (FOM) for the analysis. This is defined as

$$FOM = \frac{S^2}{S + B} \quad (3.21)$$

where S is the number of signal events and B the total number of background events, determined from Monte Carlo. We determined this using a signal portion of the M_{BC} defined by $1.865 \text{ GeV}/c^2 \leq M_{BC} \leq 1.875 \text{ GeV}/c^2$ and using a branching fraction for $D^+ \rightarrow \mu^+ \nu_\mu$ equal to what was found by the existing CLEO-c measurement [7] of 4.4×10^{-4} . The maximum figure of merit found was approximately 58, based solely on Monte Carlo.

An initial plot of the shape of the M_{BC} distribution, made before the selection cuts are applied is shown in Figure 3.15. The same plot after all of the selection cuts have been made is shown in Figure 3.16. Notice that the tails of the distribution are gone and all that remains is a narrow peak at m_D .

Chapter 4

Reconstruction Efficiency and the D Hadronic Branching Fractions

4.1 Why do we need to know the Hadronic Branching Fractions?

Using a large sample of signal Monte Carlo, we can measure the efficiency of our selection criteria with great statistical precision. However, we must also consider potential systematic sources of concern. Because we reconstruct the event completely in the hybrid neutrino reconstruction technique, the efficiency to reconstruct an event will depend very strongly on the specifics not only of the signal side of the event, but also on the decay of the D^- . And we may very well ask how well all the decays of the other side and their relative branching fractions are modeled in Monte Carlo.

At a basic level, there are three inclusive branching fractions which must be well measured and implemented in Monte Carlo in order to be able to use it to obtain an accurate efficiency calculation. The first of these is the inclusive semi-leptonic decay branching fraction $D^+ \rightarrow X\nu$, the second is the inclusive hadronic $D^+ \rightarrow K_L X$ and the last is the $D^+ \rightarrow \textit{fully visible}$; the sum of these three should be unity. Events which belong to the first group will not pass our cuts because of the presence of multiple neutrinos (and potentially because of electrons). This inclusive branching fraction is actually fairly well measured, principally because the inclusive semi-electronic branching fraction is very well measured (by CLEO-

c) [17]. Events belonging to the second group are going to fail our cuts because of the presence of the K_L in the event; even though these particles sometimes deposit some of their energy¹ there will still be two sources of missing energy and momentum in the event; the event will therefore not pass our strict reconstruction requirements. It is only events for which the entire D^- decay is fully visible that we are in going to have a reasonable efficiency to reconstruct our signal on the other side. Unfortunately, neither the branching fraction for $D^+ \rightarrow K_L X$ nor the inclusive $D^+ \rightarrow \textit{fully visible}$ are all that well known. And uncertainties in these will lead to systematic uncertainties in our efficiency measurement. Ultimately, the most important of these three is the last, since that is where we will be obtaining essentially all of our efficiency.

The additional correction to the efficiency measurement comes from the fact that the fully visible branching fraction is a sum of a large number of different branching fractions, each of which may not have the same reconstruction efficiency for our signal. One might well guess that a simple decay mode such as $D^+ \rightarrow K^- \pi^+ \pi^+$ would have a higher reconstruction efficiency than a more complicated mode such as $D^+ \rightarrow K^- \pi^+ \pi^+ \pi^0 \pi^0$.

In order to properly take all of these into account, a scheme was developed to measure all of the branching fractions of the D meson which contribute to proper reconstruction of our signal. A thorough description of this can be found in [18]; I will briefly explain the major points.

The idea is to measure all of the hadronic branching fractions of the D^+ and use this information to reweight our efficiency calculation in order to account for any errors there might be in the Monte Carlo because of improper branching frac-

¹40% of the time they leave a Splitoff approved shower, and even then it is not all of their energy

tions. By measuring the true distribution of branching fractions, we can reweight the spectrum of branching fractions in our Monte Carlo so that the efficiency calculation will use the corrected spectrum of branching fractions.

4.2 Method

We measure the branching fractions using principally the same technique that we use for our leptonic signal event reconstruction with the chief difference being that rather than looking for a signal D^+ made up of a $\mu\nu$ candidate pair, we are looking for one made up of $K^-\pi^+\pi^+$ and instead of it having large amounts of missing momentum, we restrict ourselves to looking at instances where there is very little missing energy. Specifically, our events must conform to the following criteria:

- There must be less than 100 MeV of missing energy in the event.
- *All* tracks must pass the track quality cuts mentioned in Section 3.6. Tracks which are part of a K_S candidate are not subject to requirement of d_0 and z_0 , however, since the K_S will typically have traveled some distance from the interaction point before decaying; its $c\tau$ is 2.68cm.
- The angle of the momentum of the track must be such that $|\cos\theta(\vec{p})| < 0.93$
- The π tracks on the signal side of these decays must also satisfy the “Signal Pion” criteria. These use a combination of dE/dx and RICH information to select tracks that are consistent with being a π . The dE/dx π pull must be less than 3. For pion candidates in the momentum range $650 \text{ MeV} < |\vec{p}| < 750 \text{ MeV}$ the π dE/dx pull must be less than the magnitude of the K dE/dx pull. If the RICH information for the track is good (meaning that

there are more than 3 RICH π hypothesis photons) and the momentum of the track is greater than 750 MeV, then the difference between the π and K log-likelihoods must be greater than 1 in favor of π . There is also the additional requirement that the track not be part of any K_S candidate.

- All $K_S \rightarrow \pi^+\pi^-$ candidates must have masses within ± 12 MeV of the known K_S mass.
- All other side tracks must have a dE/dx within $\pm 3 \sigma$ of the particle identification assigned to them.
- All π^0 candidates must have pull masses within the range ± 3 .
- There must be no un-vetoed extra showers in the event.
- The beam constrained mass of both the signal and the other side must fall within the range $1.8629 \text{ GeV} < M_{BC} < 1.8789 \text{ GeV}$.
- The $\Delta E_{o.s.}$ must fall within ± 300 MeV.
- the $\Delta E_{s.s.}$ must fall within ± 100 MeV. (It is obviously not possible to make a cut on $MM_{s.s.}^2$ in this situation since there is essentially no missing energy or momentum)
- The pull masses of both the D^+ and the other side D must fall within the range of ± 3 .

What this gives us is ultimately a series of yields for a very large number of different reconstructed modes on the other side. We would like to compare these with the corresponding yields from Monte Carlo so we can determine by what factors we need to reweight the various components of our Monte Carlo sample in order to get the efficiency measurement correct. However, there is an additional complication due to the fact that there will be some cross-feed between

different modes. Modes containing K_S will obviously be generally constructed using $K_S \rightarrow \pi^+\pi^-$, but there is some small chance that the $\pi^+\pi^-$ combination will fall outside the mass window of our K_S selection requirement, leading the event to be classified as a $\pi\pi$ event, rather than a K_S event. Similarly, the opposite is also true.. To obtain all the appropriate weighting factors, we write a matrix equation in terms of the ratio of the number of $D^+ \rightarrow K^-\pi^+\pi^+$ events in data to that in Monte Carlo ($N_{\text{Tag}}(\text{DATA})/N_{\text{Tag}}(\text{MC})$), the cross-feed matrix A_{ij} and the data vector of yields measured in data for each mode D_i . We must also subtract off background components from continuum yields C_i and a small number of misreconstructed tags BT_i . These last are obtained from luminosity scaling of Monte Carlo. The equation is then

$$\frac{N_{\text{Tag}}(\text{DATA})}{N_{\text{Tag}}(\text{MC})} \begin{pmatrix} A_{1,1} & A_{1,2} & \cdots & A_{1,N} \\ A_{2,1} & A_{2,2} & \cdots & A_{2,N} \\ \cdots & \cdots & \cdots & \cdots \\ A_{N,1} & A_{N,2} & \cdots & A_{N,N} \end{pmatrix} \begin{pmatrix} W_1 \\ W_2 \\ \cdots \\ W_N \end{pmatrix} = \begin{pmatrix} D_1 \\ D_2 \\ \cdots \\ D_N \end{pmatrix} - \begin{pmatrix} C_1 \\ C_2 \\ \cdots \\ C_N \end{pmatrix} - \begin{pmatrix} BT_1 \\ BT_2 \\ \cdots \\ BT_N \end{pmatrix}. \quad (4.1)$$

We float $N_{\text{Tag}}(\text{DATA})/N_{\text{Tag}}(\text{MC})$ so that the overall branching fraction for $D^+ \rightarrow K^-\pi^+\pi^+$ matches that measured by CLEO-c. To avoid combinatoric difficulties, we measure only the actual $D^+ \rightarrow K^-\pi^+\pi^+$ decays and *not* charge conjugates. The statistics are sufficiently great for the $D^+ \rightarrow K^-\pi^+\pi^+$ mode that we do not suffer any loss of precision in our final measurement as a result of this.

4.3 Counting $D\bar{D}$ pairs

For a final result we need to multiply our efficiency-divided yield by a total number of D^+ events. Rather than simply use the total number of D^+D^- events in our sample (for instance from [19]), we will use the fact that we have measured the $D^+ \rightarrow K^-\pi^+\pi^+$ yield using a technique almost identical to our analysis method. We can therefore simply take our yield divided by the $D^+ \rightarrow K^-\pi^+\pi^+$ yield as the ratio of the branching fraction for $D^+ \rightarrow \mu^+\nu_\mu$ and $D^+ \rightarrow K^-\pi^+\pi^+$. The branching fraction $\mathcal{B}(D^+ \rightarrow K^-\pi^+\pi^+) = (9.14 \pm 0.10 \pm 0.16 \pm 0.07)\%$ [19]² can be then be divided out in order to provide an absolute branching fraction for $D^+ \rightarrow \mu^+\nu_\mu$. Obviously this could potentially introduce problems because of uncertainties in the measurement of $\mathcal{B}(D^+ \rightarrow K^-\pi^+\pi^+)$; however this branching fraction is limited in the precision of its measurement purely by systematic uncertainties at this point and it is therefore not a concern for our analysis.

4.4 Measured Efficiency

The combined efficiency of all of our $D^+ \rightarrow \mu^+\nu_\mu$ selection criteria, as determined from signal Monte Carlo, is $12.10\% \pm 0.08\%_{\text{stat}}$. The efficiency The systematic uncertainties on this quantity will be divided away when we take the ratio with the $D^+ \rightarrow K^-\pi^+\pi^+$ efficiency-corrected yield. The $D^+ \rightarrow K^-\pi^+\pi^+$ efficiency is $6.89\% \pm 0.02\%_{\text{stat}}$.

²The first uncertainty is statistical, the second is all systematic uncertainties except final state radiation, and the third is the uncertainty due to final state radiation.

Chapter 5

Backgrounds

5.1 Overview

The events produced at 3770 MeV are a mixture of a variety of different types of events, all of which must be considered in terms of their contributions as backgrounds to a potential signal measurement. Obviously, CLEO-c is chiefly interested in the measurements of $D\bar{D}$ pairs, both charged and neutral, and we have measured the total cross-section for these quite precisely to be $(2.91 \pm 0.03 \pm 0.05)$ nb and $(3.66 \pm 0.03 \pm 0.06)$ nb, respectively [19]. In addition to the $D\bar{D}$ pairs, there is also light-quark continuum production, production of $\tau^+\tau^-$ and radiative returns to the $\psi(2S)$, i.e. $e^+e^- \rightarrow \psi'\gamma$. Below I will cover in detail all of the various specific processes which are significant sources of background for this analysis.

The generic continuum, $e^+e^- \rightarrow \psi'\gamma$ and $\tau^+\tau^-$ Monte Carlo samples were all of approximate $15\times$ luminosity, the generic $D\bar{D}$ sample was $30\times$ luminosity. The specific background samples generated for $D^+ \rightarrow \pi^+K_L$, $D^+ \rightarrow \pi^+\pi^0$, and $D^+ \rightarrow \tau^+\nu_\tau$ were all at least $80\times$ samples, as was the signal sample. All of the plots in this and the following chapters are normalized to the luminosity taken.

5.2 $e^+e^- \rightarrow q\bar{q}$: Continuum Production to Light quarks

The light quark continuum background is the largest background component for our analysis: it is unfortunately also the least well understood from the point of

view of Monte Carlo and other CLEO-c measurements. The total QED cross-section is easy enough to calculate as it is simply obtained using the R-value including the u , d and s quarks in all three flavors; this cross-section is 14 nb. However, there are corrections even to this total cross-section from the fact that the $\psi(2S)$ is extremely large and broad compared to the $\psi(3770)$. The tail of the $\psi(2S)$ extends all the way up to the $\psi(3770)$ and it is not understood how this interferes with the continuum production (and this interference is not included in any Monte Carlo models for the continuum). One study [20] performed to measure the resonant cross-section at the $\psi(3770)$ suggest that the total continuum cross-section is closer to 18 nb than to 14 nb; however that particular measurement was concerned with finding ways of canceling the non- $\psi(3770)$ contribution rather than calculating its size and so nothing more than an estimate was ever obtained.

Beyond simply knowing the total cross-section, there is the question of the structure of continuum production and how it is modeled in Monte Carlo. All current generation Monte Carlo uses JETSET [21]. This is not tuned for running at low energies such as the conditions found at CLEO-c. The track multiplicities, momentum spectra, shower spectra and multiplicities have only been tested to a crude approximation. For the purposes of most other CLEO-c analysis, the light quark continuum background has been negligibly small and therefore not been a major concern; people have generally been able to count it as below a measurable contribution. This analysis is thus the first time that anyone has had to take a close look at continuum production as it relates as a background to a D meson decay process.

Ultimately, this led to the decision to not rely on the Monte Carlo for the continuum at all in any significant way. Obviously there are some general fea-

tures which were used, such as the fact that it peaks strongly towards ± 1 in $\cos \theta$ (see Figure 5.1), leading to the selection criterion for the direction of the missing momentum mentioned in section 3.10.

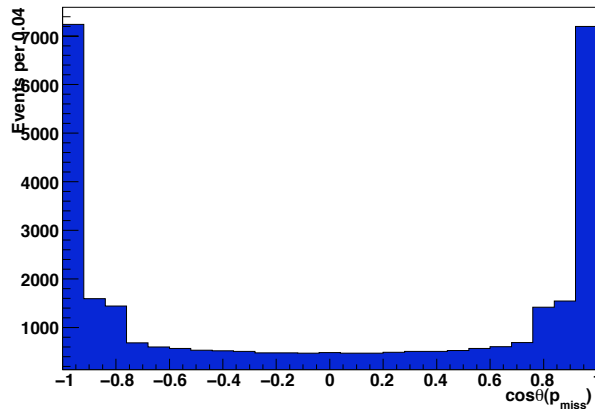


Figure 5.1: Distribution of $\cos \theta$ of \vec{p}_{miss} for continuum MC. Note the very strong peaking towards ± 1 .

Based on the Monte Carlo, we are also able to state that there is essentially no structure in any of the other variables which we use to discriminate, as is obvious from Figures 5.2 and 5.3. There is some very broad peaking behavior, but this is not significant.

The M_{BC} distribution is of particular interest, since it's what we will be fitting in, and we can see that both with and without our event selection cuts (Figures 5.5 and 5.4, respectively), it has the general shape which can be parameterized by an ARGUS function [22]. This can be written as

$$f(x) = x \left[1 - \left(\frac{x}{m_0} \right)^2 \right]^p \exp \left\{ c \left[1 - \left(\frac{x}{m_0} \right)^2 \right] \right\} \quad (5.1)$$

where m_0 is the cutoff energy, c is the curvature and p is the power (which for the original ARGUS function is equal to 0.5, but which we will allow to float as a free parameter).¹ We will not use the Monte Carlo to determine these parameters in

¹Note that by this definition the curvature c will generally be negative. This convention is

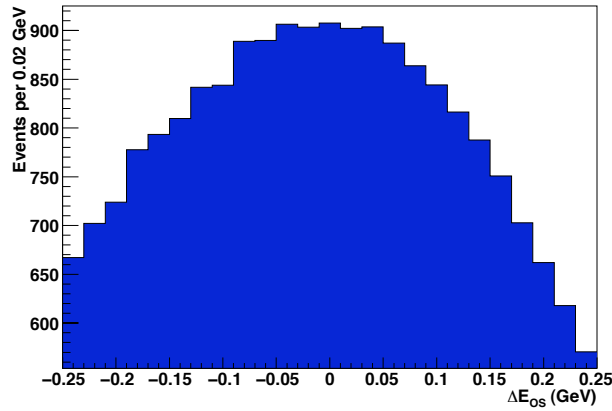


Figure 5.2: $\Delta E_{o.s.}$ for continuum MC with very loose cuts; there is no narrow peaking structure.

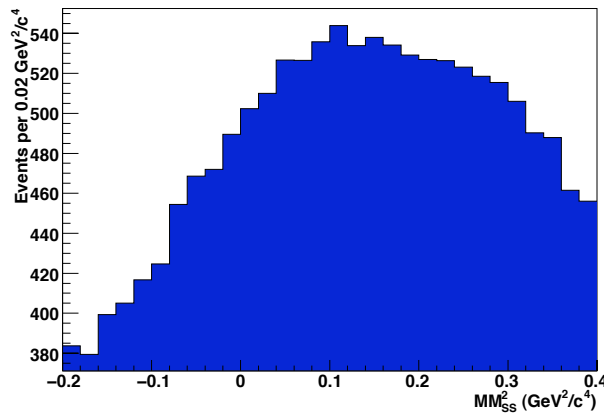


Figure 5.3: $MM_{s.s.}^2$ for continuum MC with very loose cuts; there is no narrow peaking structure.

the way that we will for other background components, but we will use the fact that we can parameterize the continuum contribution as *an* ARGUS function when fitting the data. This is explained in more detail in section 6.3.5.

chosen because it is the choice made by RooFit [23]

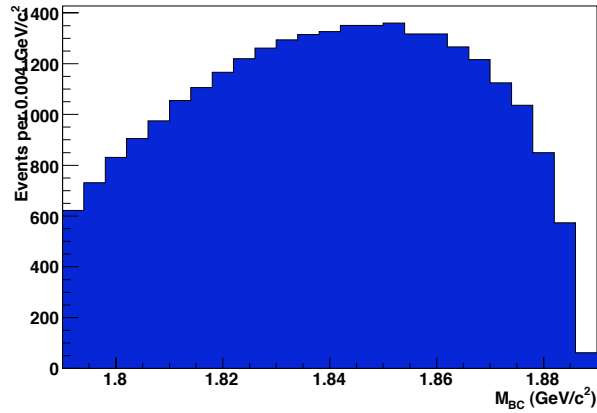


Figure 5.4: M_{BC} for continuum MC with only very loose cuts. Note the basic ARGUS shape.

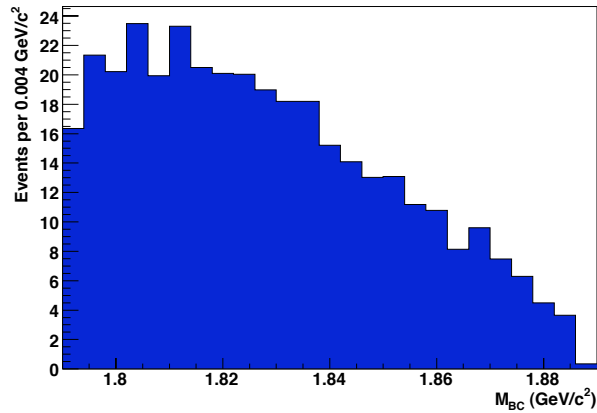


Figure 5.5: M_{BC} for continuum MC which has passed our selection criteria.

5.3 $e^+e^- \rightarrow \psi'\gamma$: Radiative Returns

The cross-section for radiative returns to the $\psi(2S)$ (the $\psi(2S)$ and the ψ' are different naming conventions for the same state) has been measured by CLEO to be 3.31 nb [24]. While this is small, the fact that there is inherently a large amount of missing energy and momentum in these events (because of the initial state photon) means that there is the potential for these events to mimic our

signal. Because of this relatively high energy initial state photon, these events need to have some other missing particle in them, typically a K_L , if the direction of the missing momentum is not going to point down the beam pipe. It is clear from Figure 5.6 that the missing momentum does strongly favor pointing in the direction of $\cos \theta = \pm 1$, meaning that most of the events from this process will be eliminated by the same criterion used to eliminate the continuum background.

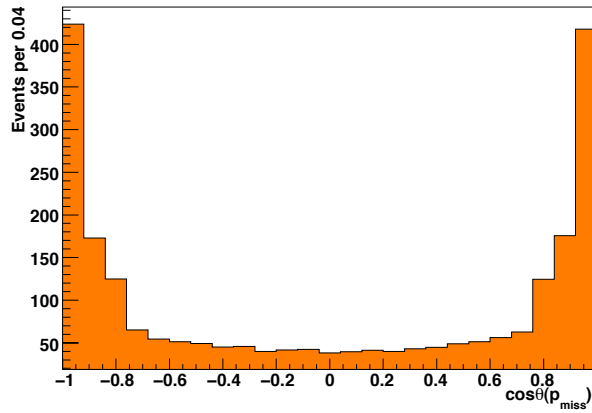


Figure 5.6: Distribution of $\cos \theta$ of \vec{p}_{miss} for radiative return MC. This peaks strongly towards ± 1 .

Since radiative return events contain no real D mesons, our criteria used to eliminate poorly reconstructed signal and other-side D 's are very effective. If we look at pre-selection distributions of $MM_{\text{s.s.}}^2$ (Figure 5.3) and $\Delta E_{\text{o.s.}}$ (Figure 5.7), it is clear that there is no peaking structure in either of them. Furthermore, since the processes do not stem from the decay of real D mesons, they are not correlated: cuts on one variable will not affect the distribution of the other.

If we consider the M_{BC} distribution before and after the selection criteria are made (Figures 5.9 and 5.10), we can see the dramatic reduction effect, making sure to note the vertical scale. In both cases, the number of events is normalized to the

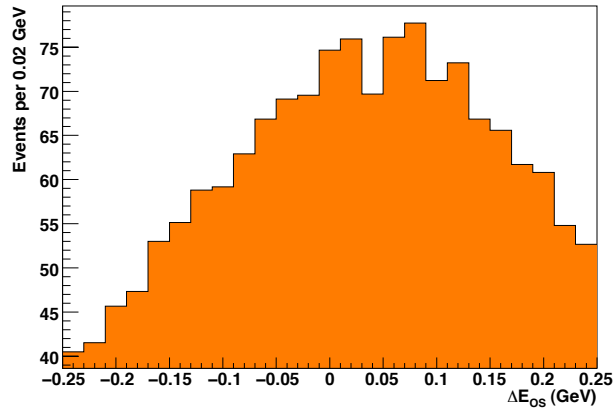


Figure 5.7: $\Delta E_{o,s.}$ for radiative returns Monte Carlo.

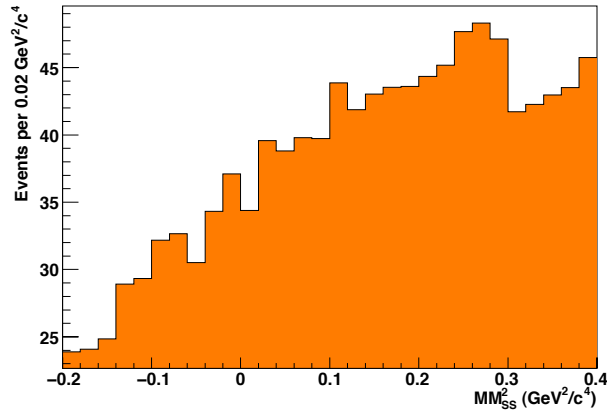


Figure 5.8: $MM_{s,s}^2$ for radiative returns Monte Carlo.

full luminosity, based on the cross-section of 3.31 nb. It is worth noticing that even with the relatively coarse binning used in Figure 5.10, there are clearly problems because of low statistics with this particular background component, more so than with others.

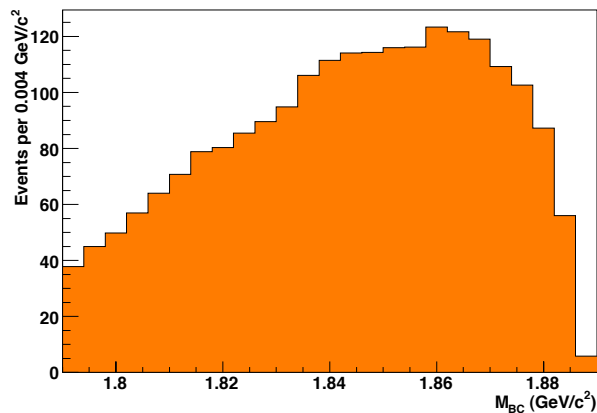


Figure 5.9: M_{BC} for radiative return MC before cuts.

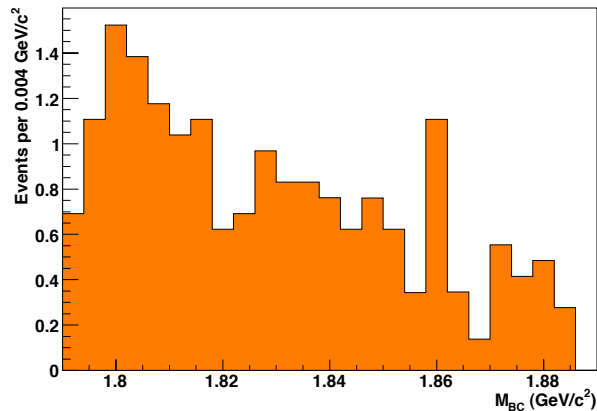


Figure 5.10: M_{BC} for radiative return MC after cuts.

5.4 $e^+e^- \rightarrow \tau^+\tau^-$: τ -Pair Production

The production of $e^+e^- \rightarrow \tau^+\tau^-$ is a QED process which is well understood and CLEO has implemented excellent models of this using KORALB [25] in addition to the usual event generators. The cross-section for this process is 2.73 nb (from a KORALB calculation). While this is even slightly smaller than that of the radiative returns, the fact that both tau particles decay to final states including at least one neutrino means that this process can contribute a larger background to our signal.

This is also the only bulk background process which yields a missing momentum vector which is not generally pointing towards the endcaps, but is instead evenly distributed in $\cos\theta$, as is shown in Figure 5.11. Not only is the missing momentum created by real neutrinos, but because there are two taus in the initial state, there must be at least two neutrinos in the final state, and given the many decay modes of τ leptons, there will generally be more than just two neutrinos. This means that the direction of the missing momentum is not biased towards the end caps.

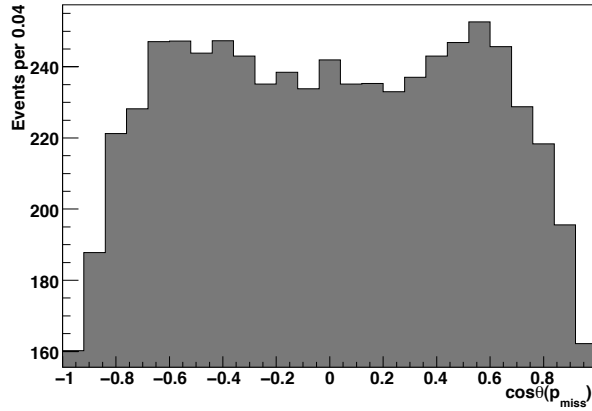


Figure 5.11: Distribution of $\cos\theta$ of \vec{p}_{miss} for τ -pair MC. Note that it does not peak towards ± 1 .

Much the same reasoning holds for $\tau^+\tau^-$ as does for radiative returns in some respects, however: the observed $\mu - \nu$ combination is not coming from any sort of real D meson decay, and we therefore don't expect any of the kinematic variables describing them to be peaking. The same will hold for whatever D^- we reconstruct on the 'other side'; it will not be from a real decay process. This is shown in Figures 5.12 and 5.13.

The effects of our event selection criteria has a similar effect on the background overall as well, as is shown in Figures 5.14 and 5.15. Notice that although the

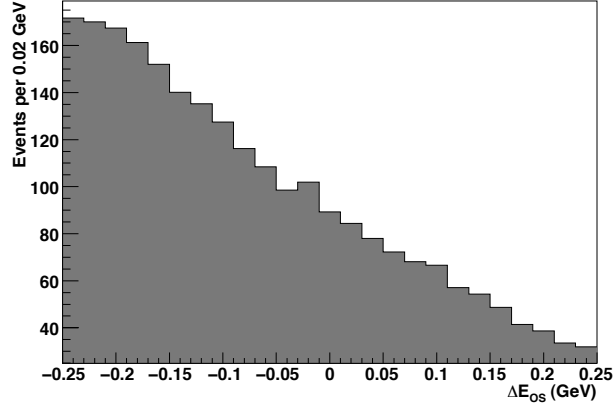


Figure 5.12: $\Delta E_{\text{o.s.}}$ for τ -pair MC without cuts. There are neutrinos in the decays on *both* sides of the event, so there will be less energy left over to create a D^- -candidate, hence the shape of this plot.

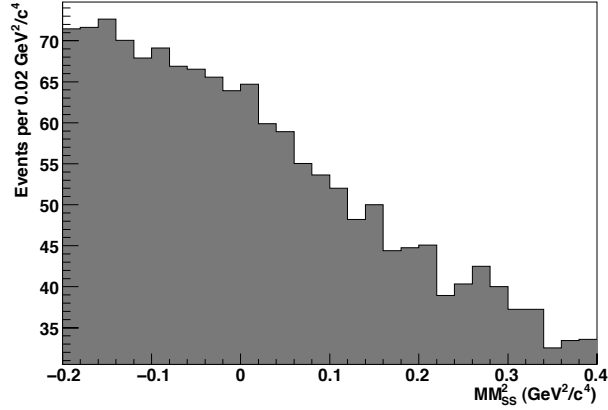


Figure 5.13: $MM_{\text{s.s.}}^2$ for τ -pair MC without cuts. The shape is created by the presence of multiple ν 's in the event.

overall cross-section for the process is lower than for radiative returns, more events will pass both the very loose initial selection criteria (to be in Figure 5.14) and our final cuts because the events all have large amounts of missing energy and momentum in them, causing them to be more likely to mimic our signal.

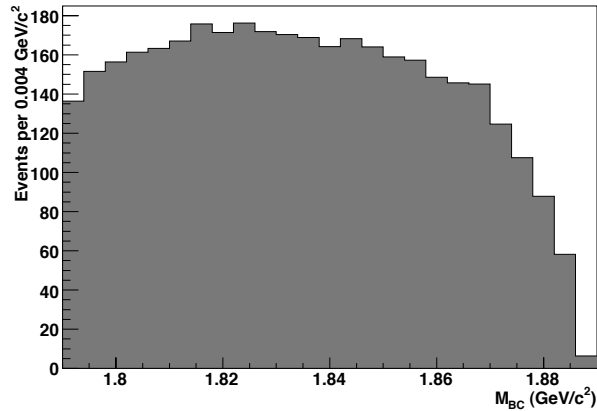


Figure 5.14: M_{BC} for τ -pair MC before our event selection criteria.

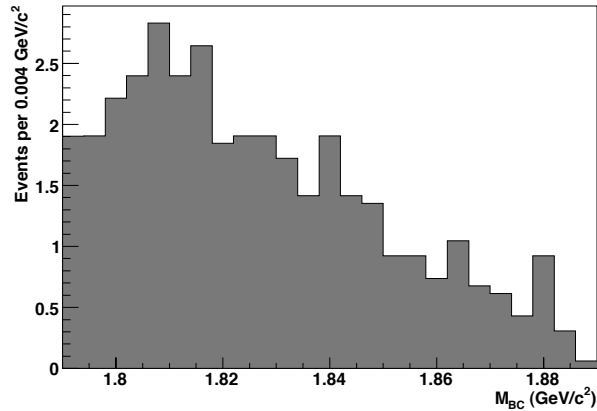


Figure 5.15: M_{BC} for τ -pair MC after our event selection criteria.

5.5 $D\bar{D}$ -Pairs

$D\bar{D}$ -pairs contribute to the background in a variety of ways, although there are three dominant decay modes which provide the majority of the contribution. These are all decays of the D^+ , meaning charged and the same sign as the signal. The contribution from neutral pairs is small and comes mainly from semi-leptonic decays with lost particles, or hadronic decays with lost particles. This can also occur in the case of charged semi-leptonic decay, generally where there are extra lost

photons or where the hadron is somehow attributed to coming from the D^- . However, the missing momentum is much larger for this analysis than for a typical semi-leptonic decay that it is therefore fairly difficult for a semi-muonic decay to mimic the signal. Overall, aside from the three specific modes mentioned below, this background is dominated by mis-reconstructed events with lost showers and tracks.

The three major decay modes of the D^+ that are backgrounds for our mode are $D^+ \rightarrow \pi^+ K_L$, $D^+ \rightarrow \pi^+ \pi^0$, and $D^+ \rightarrow \tau^+ \nu_\tau$ (which is followed immediately by $\tau^+ \rightarrow \pi^+ \bar{\nu}_\tau$). The first two are both two-body decays of the D^+ , like our signal, and since it is easy for pions to fake as muons, all that remains is for the K_L or π^0 to masquerade as a neutrino. The third mode can be viewed as a type of signal, but not one we can actually look for. $D^+ \rightarrow \tau^+ \nu_\tau$ is not something our search is sensitive to, but does appear as a background. What we term ‘generic’ $D\bar{D}$ backgrounds are what are not accounted for by our three specific modes: these tend to be hadronic, although some semi-leptonic modes do contribute at a small level. They almost all result from misidentified π^+ particles combined randomly with lost showers, particles, or K_L ’s.

The generic $D\bar{D}$ decays also peak towards the end-caps, albeit less strongly than radiative returns or continuum, as shown in Figure 5.16; this means that the cut on the direction of \vec{p}_{miss} will also suppress this background contribution. The $MM_{\text{s.s.}}^2$ distribution (Figure 5.17 does not show any real structure beyond a simple monotonic increase with increasing $MM_{\text{s.s.}}^2$, showing that this is dominated by lost showers and particles. The same is the case with the distribution of $\Delta E_{\text{o.s.}}$ (Figure 5.18, showing a very small peak at zero, indicating events which are well reconstructed on the other side. For the most part, however, the events are not,

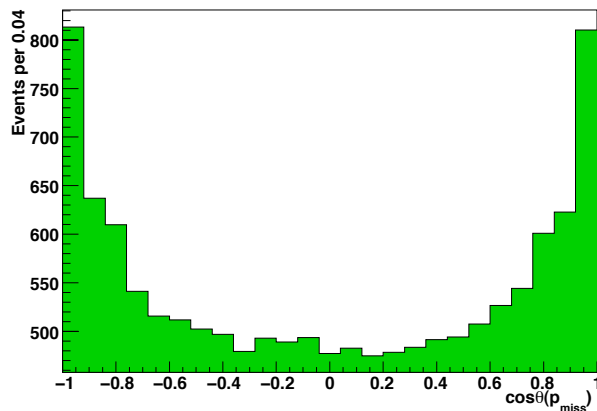


Figure 5.16: Distribution of $\cos \theta$ of \vec{p}_{miss} for generic $D\bar{D}$ MC. It also peaks towards the direction of the beam pipe because of lost particles and showers.

and these will be eliminated by our selection criteria.

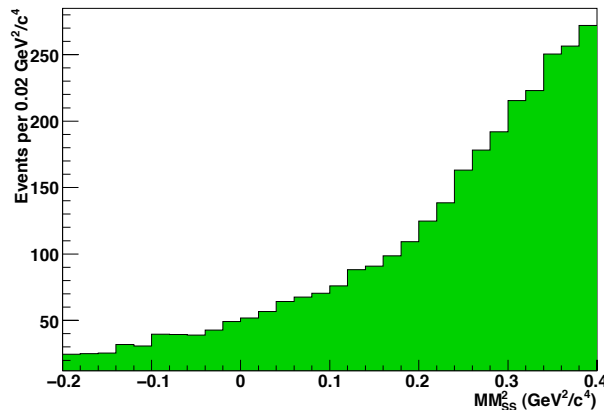


Figure 5.17: $MM^2_{\text{s.s.}}$ for ‘generic’ $D\bar{D}$ MC with the loosest possible cuts. There is no real structure other than a monotonic increase towards higher $MM^2_{\text{s.s.}}$.

The vertical scale on the $D\bar{D}$ M_{BC} distributions before and after cuts (Figures 5.19 and 5.20, respectively) show the dramatic effect of our selection criteria once again. The distribution after cuts is dominated by combinatoric misreconstructed events, typically including multiple lost particles. Remember that

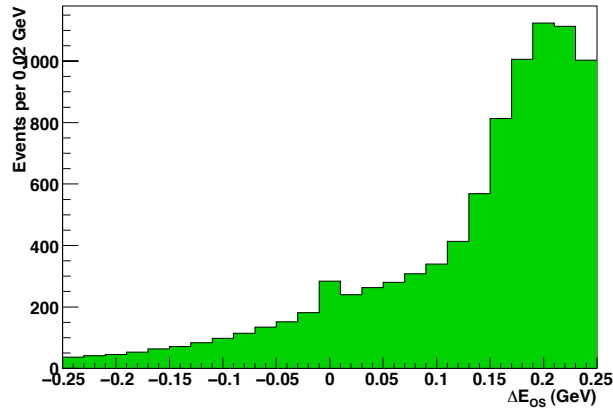


Figure 5.18: $\Delta E_{o.s.}$ for ‘generic’ $D\bar{D}$ MC with the loosest possible cuts. There is no real structure other than a monotonic increase towards higher $\Delta E_{o.s.}$.

the main peaking contributions are being considered separately (see below) and what is included here is essentially all the ‘junk’ that somehow slips through the cuts.

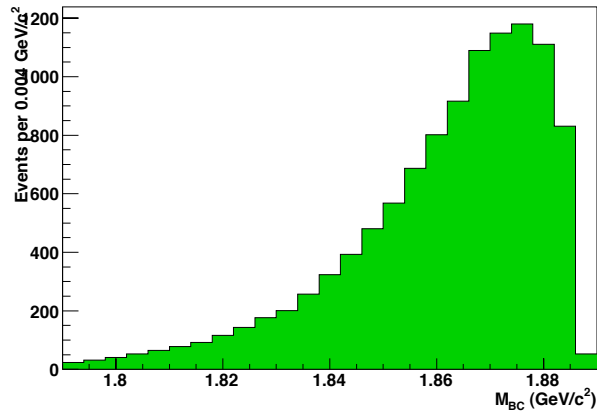


Figure 5.19: M_{BC} for generic $D\bar{D}$ MC before our event selection criteria.

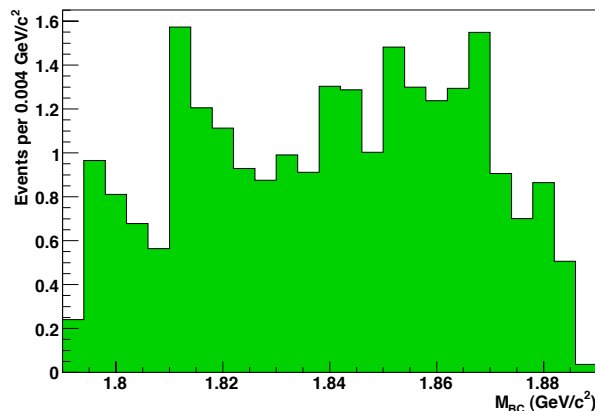


Figure 5.20: M_{BC} for generic $D\bar{D}$ MC after our event selection criteria.

5.5.1 $D^+ \rightarrow \pi^+ K_L$

The cross section for this decay has been measured by CLEO-c to be $1.460 \pm 0.040 \pm 0.035\%$ [26] and this mode superficially resembles our signal in a number of ways. However, despite the large magnitude of the cross-section, there are some fairly straightforward ways for us to reduce this background's contribution to our measurement.

The first thing to note about these events is that they are reconstructed from *real* decays of D mesons on both sides of the event. This means that our selection criteria designed to filter out poorly reconstructed D candidates, particularly on the other side, will not be very effective: this is shown clearly in Figure 5.21. Actually, the use of the improved neutrino reconstruction technique will enhance this background mode much in the way that it enhances the signal mode, simply because it's cleaning up the reconstruction of the other side D .

Looking at the signal side, it is fortunately the case that $D^+ \rightarrow \pi^+ K_L$ events will not, yield the correct $MM_{s.s.}^2$, as shown in Figure 5.22. The particle leading to

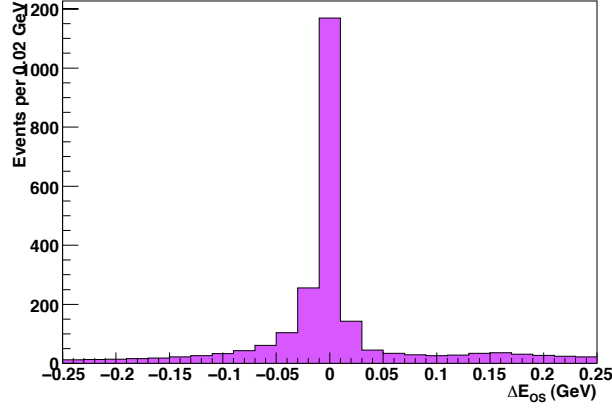


Figure 5.21: $\Delta E_{o.s.}$ for $D^+ \rightarrow \pi^+ K_L$ MC with the loosest possible cuts; the other side is well reconstructed for these events.

the missing energy and momentum is in fact a K_L instead of a ν , and if correctly reconstructed there will be a $MM_{s.s.}^2 = m_K^2$ rather than $MM_{s.s.}^2 = 0$. We will therefore be able to eliminate much of this background contribution with our criterion that $-0.08 \text{ GeV}^2/c^4 < MM_{s.s.}^2 < 0.08 \text{ GeV}^2/c^4$.

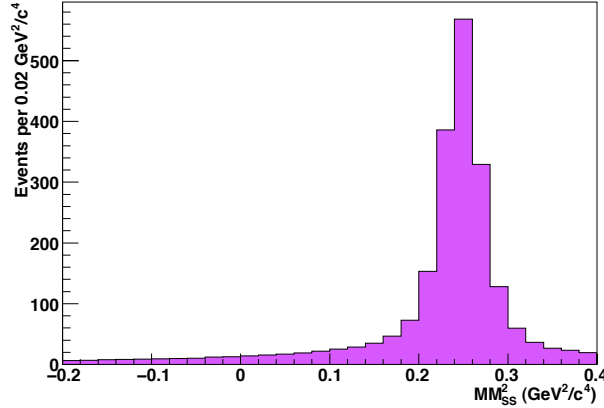


Figure 5.22: $MM_{s.s.}^2$ for $D^+ \rightarrow \pi^+ K_L$ MC with the loosest possible cuts. Note the large peak at $0.25 \text{ GeV}^2/c^4$, the K_L mass.

The M_{BC} distribution for this background before cuts looks very like our signal in terms of shape before the selection criteria are applied (Figure 5.23). After all of our cuts have been applied, however, it looks rather different in shape, as shown

in Figure 5.24. This means that, like for the generic $D\bar{D}$ background, we will have to model its shape in a more sophisticated way than using a simple functional form.

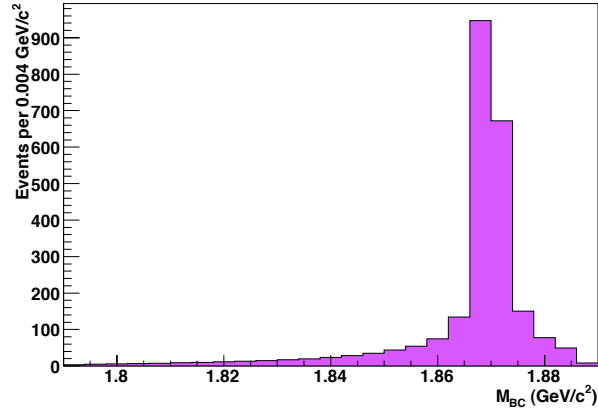


Figure 5.23: M_{BC} for $D^+ \rightarrow \pi^+ K_L$ MC with the loosest possible cuts; it looks very like signal.

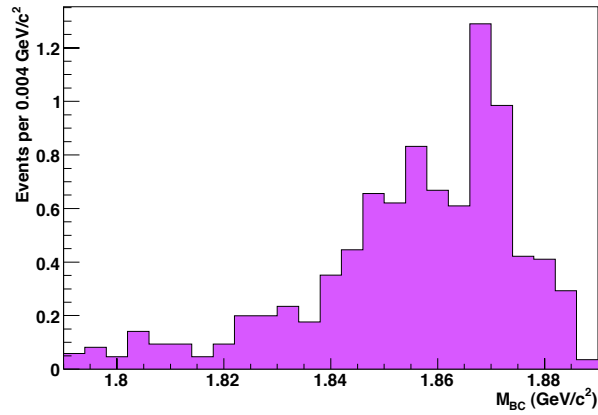


Figure 5.24: M_{BC} for $D^+ \rightarrow \pi^+ K_L$ MC with all our selection cuts; it now has a complex shape.

5.5.2 $D^+ \rightarrow \pi^+\pi^0$

This is another process with a well measured branching fraction of $(1.28 \pm 0.09) \times 10^{-3}$ [13]. However, it is potentially a major contaminant since it is a two-body decay which could look very like our signal. The π^+ can obviously pass our minimum ionizing requirements half of the time, and one might well think that the largest danger posed by this background source was from the situation in which the π^0 escaped down the beam pipe. However, we already know that our cut on the direction of \vec{p}_{miss} will take care of that.

If we look at the $\Delta E_{\text{o.s.}}$ variable before any such cuts are made, we see that it has a large peak at zero, as we would expect, but we also note that there are rather long tails (Figure 5.25). The source of these becomes clear when we look at the $MM_{\text{s.s.}}^2$ plot (Figure 5.26), where we see not one, but two large peak.

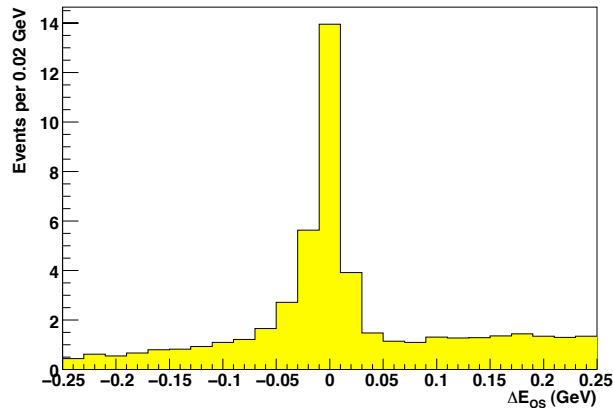


Figure 5.25: $\Delta E_{\text{o.s.}}$ for $D^+ \rightarrow \pi^+\pi^0$ MC with loose cuts. there are large broader tails than for signal MC.

The first peak is at a value equal to $m_\pi^2 \simeq 0.02 \text{ GeV}^2/c^4$, while the other peak is at $m_K^2 \simeq 0.25 \text{ GeV}^2/c^4$. What this tells us is that it is not always the case that the π^+ is being paired with the lost π^0 ; some of the time it is paired with a

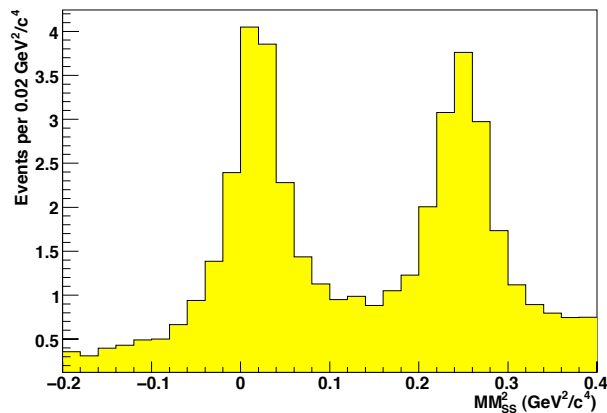


Figure 5.26: $MM_{s.s.}^2$ for $D^+ \rightarrow \pi^+\pi^0$ MC with the loosest possible cuts. Note the peaks at both 0.02 and 0.25 GeV^2/c^4 .

K_L from the other side of the event and the combinatorics of the event are such that the π^0 combine with the rest of the other side in order to make a decent D^- candidate (although not one with a perfect $\Delta E_{o.s.}$). This is obviously a rare occurrence, but not significantly more rare than losing both photons from the π^0 . Note, of course, that the peak at m_K^2 will be removed once we apply our selection criteria, since it falls outside our signal window, whereas the peak at 0.02 GeV^2/c^4 falls within the cut range.

If we look at the M_{BC} distribution after we have made our selection cuts, we see that it looks exactly like our signal, but that it is a small contribution, as shown in Figure 5.27. We will fit it using a double Gaussian, as discussed in section 6.3.4.

5.5.3 $D^+ \rightarrow \tau^+\nu_\tau$

Under ideal circumstances, we would like to be able to measure the decay $D^+ \rightarrow \tau^+\nu_\tau$; however this is not possible because it has a branching fraction only

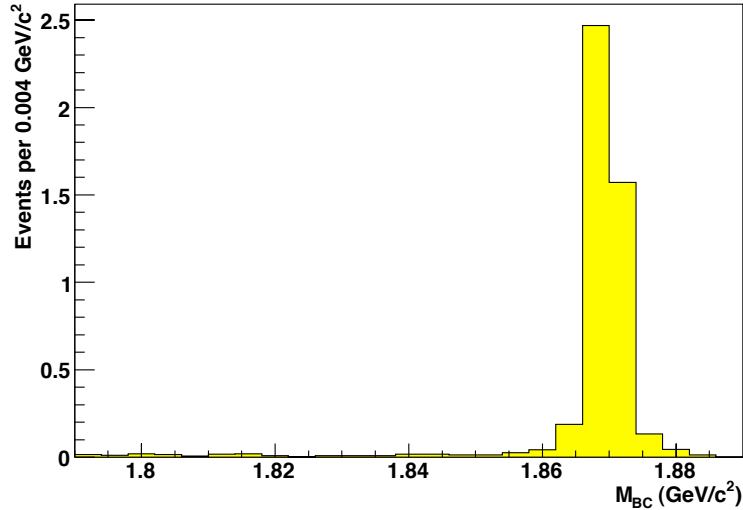


Figure 5.27: M_{BC} for $D^+ \rightarrow \pi^+\pi^0$ MC with all our cuts; it looks just like signal.

slightly larger than our signal (by a factor of 2.65 in the standard model) and the branching fraction for $\tau^+ \rightarrow \pi^+\bar{\nu}_\tau$ is only $10.90 \pm 0.07\%$ [13]. Furthermore, because there are two neutrinos in the final state, it is slightly less clean than our $D^+ \rightarrow \mu^+\nu_\mu$ signal. The other side is no less clean than our signal, however, and as such the D^- will be reconstructed properly, as shown in Figure 5.28. Similarly, the M_{BC} distribution looks very like the signal distribution, both before and after selection cuts (see Figures 5.29 and 5.30).

The reason for the decrease in the magnitude of the peak comes from looking at the $MM_{\text{s.s.}}^2$ plot, which does not peak at zero but ends up looking very broadly smeared out, as is shown in Figure 5.31. The fact that there are two neutrinos instead of just one means that, unless they are perfectly collinear, they will have a non-zero invariant mass. The shape of that invariant mass distribution is what it seen in Figure 5.31. Note that it has something of a cut-off at zero (on top of some less clean background), corresponding to when the two neutrinos are in

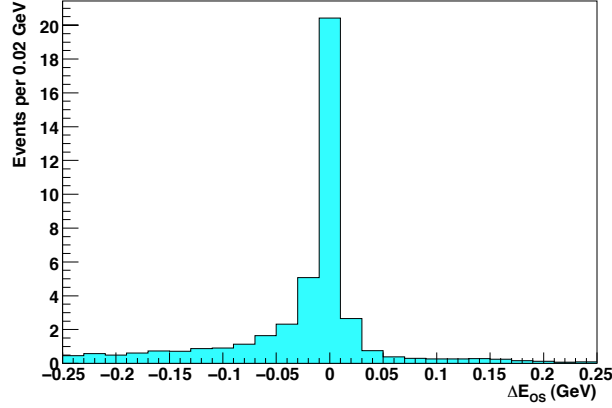


Figure 5.28: $\Delta E_{o.s.}$ for $D^+ \rightarrow \tau^+ \nu_\tau$ MC with the loosest possible cuts; it looks exactly like signal MC.

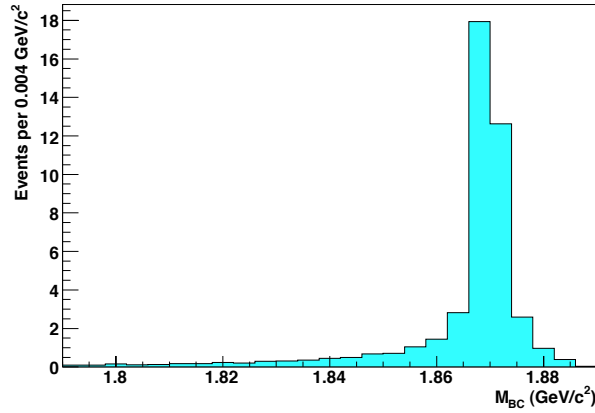


Figure 5.29: M_{BC} for $D^+ \rightarrow \tau^+ \nu_\tau$ MC with the loosest possible cuts, resembling signal MC.

fact collinear. The rest of the distribution smeared towards the positive direction corresponds to the neutrinos being less and less collinear, resulting in a greater and greater invariant mass.

We will fit this background as a double Gaussian and fix its contribution based on the measured signal what should be expected given the standard model prediction of the ratio of the $D^+ \rightarrow \mu^+ \nu_\mu$ and $D^+ \rightarrow \tau^+ \nu_\tau$ branching fractions. While

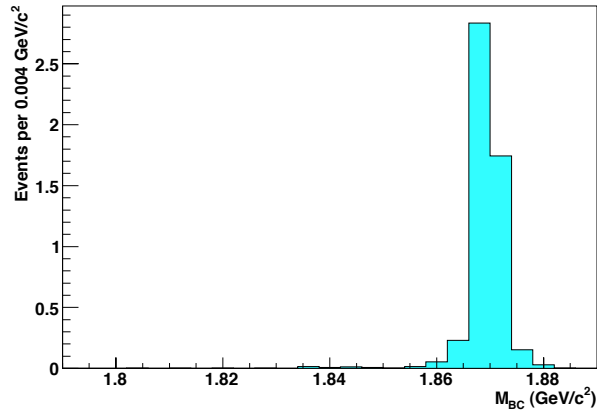


Figure 5.30: M_{BC} for $D^+ \rightarrow \tau^+ \nu_\tau$ MC after all cuts, greatly diminished in magnitude.

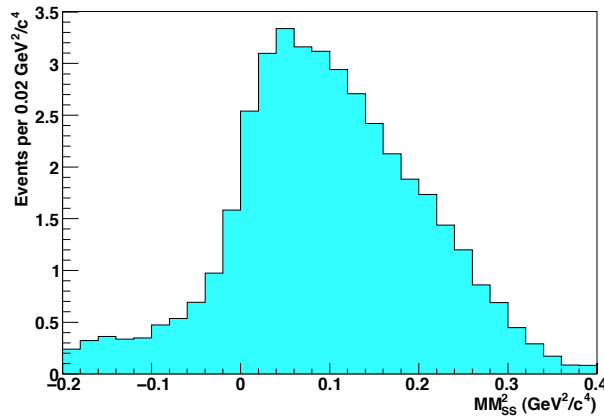


Figure 5.31: $MM_{s.s.}^2$ for $D^+ \rightarrow \tau^+ \nu_\tau$ MC with the loosest possible cuts. The peak is broadly smeared from zero in the positive direction.

this does not give us sensitivity to physics beyond the standard model, it does give us a better measure on this background, and any such sensitivity would be negligible in any case.

Chapter 6

Fitting

6.1 Overview

We fit the data using models of the Monte Carlo for the signal and background after we have applied all of the selection criteria mentioned in Chapter 3. The fitting was done using the RooFit software package [23] as an integrated part of the Root environment [27]. The plots in the following sections (used for generating PDFs) are *not* normalized in order to make use of the full statistics of the Monte Carlo samples available. In all cases, the fits were done using a maximum likelihood-technique. As previously stated, we use the M_{BC} variable to fit in.

6.2 Signal Fitting

We fit the signal Monte Carlo using a double Gaussian shape (meaning a sum of two Gaussians), as this was the simplest shape that fit the data well. More complicated shapes such as three Gaussians, two Crystal Ball functions [28] (with a tail in either direction), or the sum of a Gaussian and a bifurcated Gaussian (different mean in each direction) did not fit the function better than a simple double Gaussian. The fit to a MC signal sample is shown in Figure 6.1 and the parameters from it are shown in Table 6.1. Only a limited region is used so as to give a higher quality fit; if the entire region 1.79–1.89 is used, the quality of the fit degrades.

Table 6.1: The parameters for the fit to the signal Monte Carlo, used to determine the shape of the signal peak in the final fit.

Primary Gaussian \bar{x}_1	1689.49 MeV	± 0.014 MeV
Primary Gaussian σ_1	1.43 MeV	± 0.017 MeV
Secondary Gaussian \bar{x}_2	1870.24 MeV	± 0.062 MeV
Secondary Gaussian σ_2	3.66 MeV	± 0.078 MeV
Fraction in First Gaussian	0.75	± 0.01

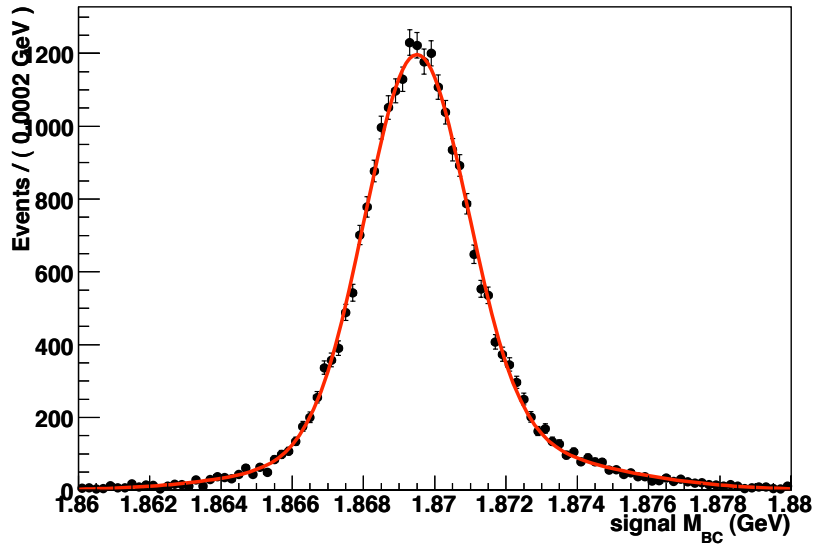


Figure 6.1: A fit of the signal Monte Carlo to a sum of two Gaussians.

6.3 Background Fitting

The different backgrounds are also all fitted from Monte Carlo, with the exception of continuum, which is fitted purely from the data, as mentioned in section 5.2. Each of the different background components is fitted separately using a combination of ARGUS and Gaussian functions. The parameters found from fitting are all shown in Table 6.2. These are then used (as fixed values) in the combined fit. The normalized yields (as taken from cross-section measurements listed in the previous

chapter) are also used as fixed parameters in the combined fit.

6.3.1 $e^+e^- \rightarrow \psi'\gamma$ and $\tau^+\tau^-$

The small contribution from $e^+e^- \rightarrow \psi'\gamma$ and $e^+e^- \rightarrow \tau^+\tau^-$ are individually modeled using an ARGUS function in which we fix the cut-off energy to be the beam energy and allow both the curvature c and the power p to float. The results are shown in Figures 6.2 and 6.3. As previously mentioned, these plots are not normalized. The normalized yields for these processes in the range 1.79–1.89 are set by the QED cross section of 2.73 nb (as calculated using KORALB) for the $e^+e^- \rightarrow \tau^+\tau^-$ [25], and from the CLEO-c measurement of the $e^+e^- \rightarrow \psi'\gamma$ cross-section of 3.31 nb [24] and are 18.15 ± 1.15 and 35.99 ± 1.49 , respectively.

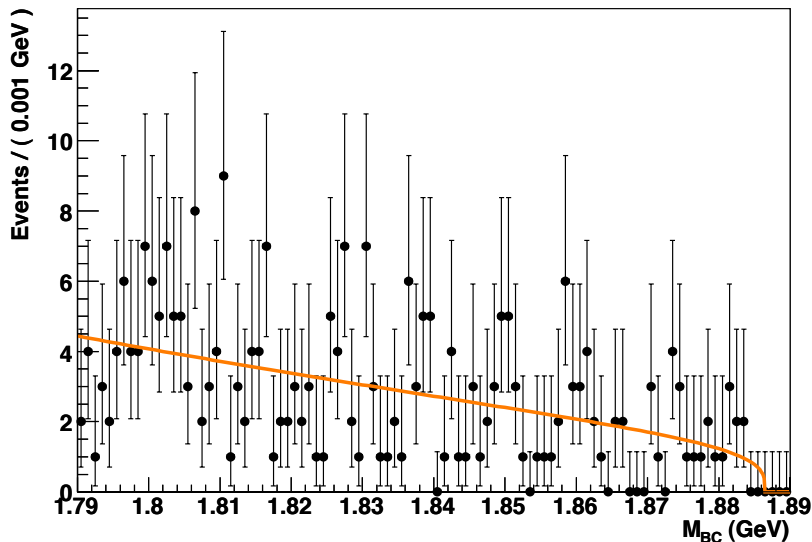


Figure 6.2: A fit of the $e^+e^- \rightarrow \psi'\gamma$ Monte Carlo to an ARGUS function.

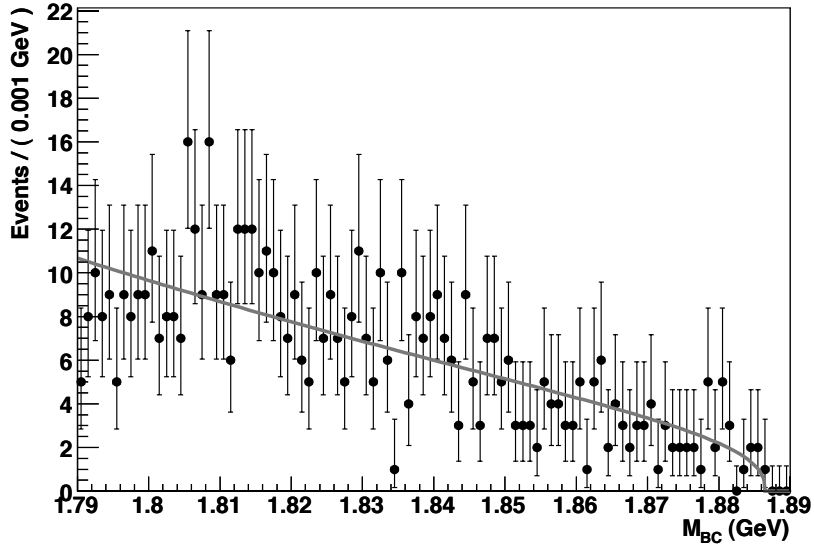


Figure 6.3: A fit of the $e^+e^- \rightarrow \tau^+\tau^-$ Monte Carlo to an ARGUS function.

6.3.2 $D\bar{D}$ -pairs

As mentioned in Section 5.5 and as was shown in Figure 5.20, the shape of the generic $D\bar{D}$ backgrounds is such that it can be roughly parameterized by using an ARGUS-like function. The reason for using this particular function is principally to include the cut-off at the beam-energy, something which would not be done if one were to use a histogram smoothing or interpolation algorithm. The results are shown in Figure 6.4. The normalized yield is obtained by using the total cross-section measured by CLEO-c [19] and is 29.36 ± 1.02 .

6.3.3 $D^+ \rightarrow \pi^+ K_L$

Because the $D^+ \rightarrow \pi^+ K_L$ shows structure beyond a simple peak or a simple ARGUS shape, we must fit this component using a combination of functions. We

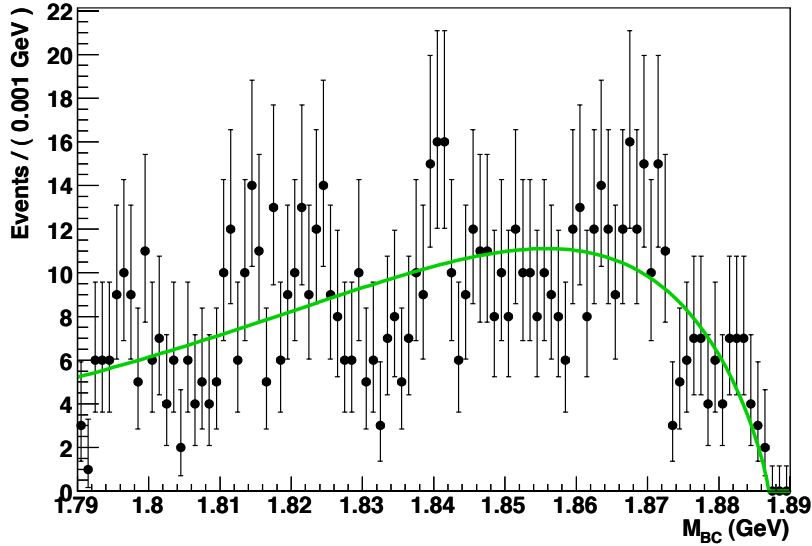


Figure 6.4: A fit of the generic $D\bar{D}$ -pairs Monte Carlo using an ARGUS function.

choose to fit it using a Gaussian shape to model the peaking structure and an ARGUS shape to model the non-peaking portion of the background. This allows us to fit the shape of the distribution reasonably well, as is seen in Figure 6.5. There is a small shoulder in the distribution which is not well represented in the fitting function, but since the normalized yield for this background is quite small, this does not have a large impact. The yield is fixed by the CLEO-c measured cross-section for $D^+ \rightarrow \pi^+ K_L$ [26], and is 9.178 ± 0.329 .

6.3.4 $D^+ \rightarrow \pi^+ \pi^0$ and $D^+ \rightarrow \tau^+ \nu_\tau$

These background components both look very like our signal after we have made all of the selection requirements and we fit them in the same way as we fit our signal; using a double Gaussian. Furthermore, we only fit looking at the narrower region of 1.86–1.88 so as to get a higher quality fit. That is the only region in which they

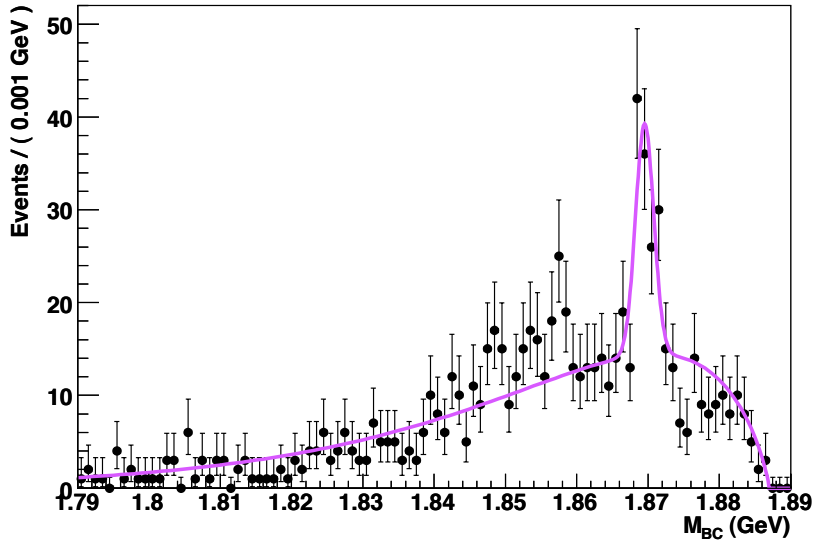


Figure 6.5: A fit of the $D^+ \rightarrow \pi^+ K_L$ Monte Carlo using a Gaussian plus an ARGUS function.

contribute and we wish to make the best possible functional fit to their shape. They fit the double Gaussian shape very well, as may be seen from Figures 6.6 and 6.7, which show the $D^+ \rightarrow \pi^+ \pi^0$ and $D^+ \rightarrow \tau^+ \nu_\tau$ fits, respectively. The contribution from $D^+ \rightarrow \pi^+ \pi^0$ is fixed in yield from Monte Carlo using the PDG branching fraction for $D^+ \rightarrow \pi^+ \pi^0$ [13] and is 4.710 ± 0.0984 . The $D^+ \rightarrow \tau^+ \nu_\tau$ yield, on the other hand, is floated with the signal in such a way that the ratio between the $D^+ \rightarrow \mu^+ \nu_\mu$ and $D^+ \rightarrow \tau^+ \nu_\tau$ yields are fixed (calculated from the standard model). This contribution can then be subtracted from the signal peak after the final yield is obtained from the global fit.

6.3.5 Continuum

The one background whose yield and shape we are not determining in advance using Monte Carlo is the light quark continuum, as was discussed in section 5.2.

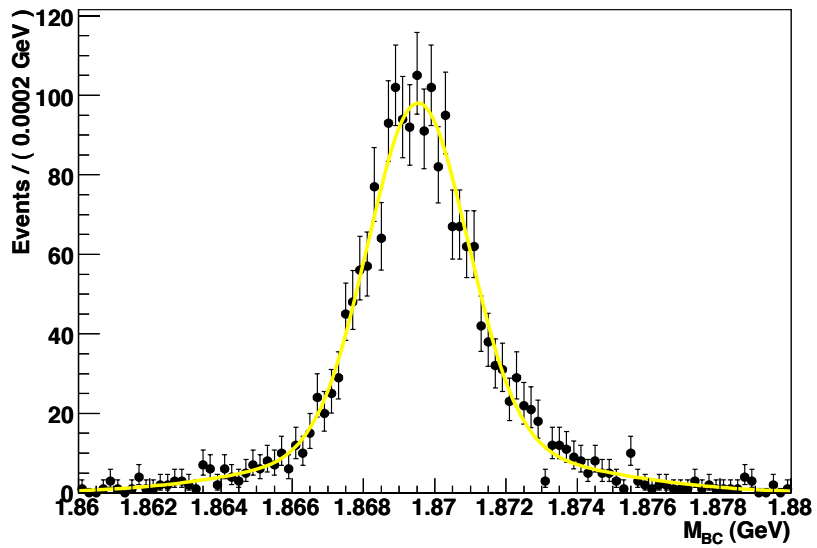


Figure 6.6: A fit of the $D^+ \rightarrow \pi^+ \pi^0$ Monte Carlo using two Gaussians.

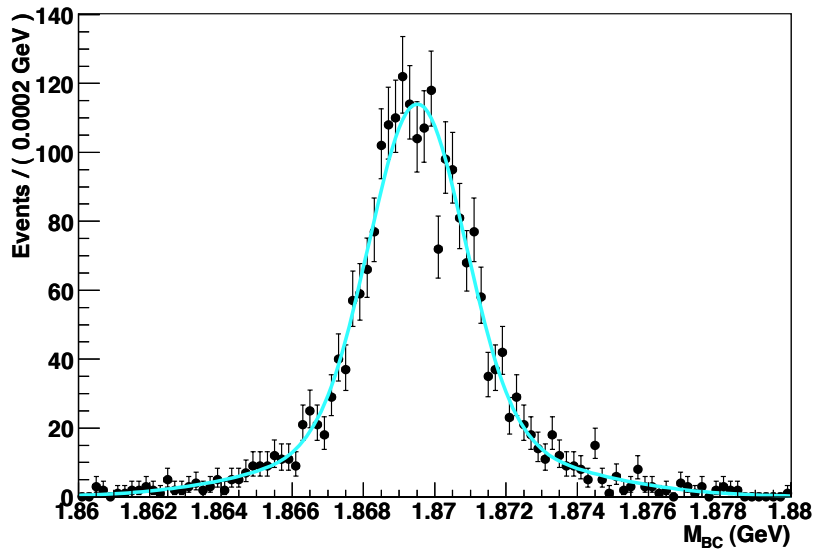


Figure 6.7: A fit of the $D^+ \rightarrow \tau^+ \nu_\tau$ Monte Carlo using two Gaussians.

Table 6.2: The parameters for all the different fitted portions of the background, obtained from Monte Carlo.

$e^+e^- \rightarrow \psi'\gamma$	Cutoff m_0	1887.0 MeV	Fixed
	Curvature c	5.4	± 5.3
	Power p	0.32	± 0.20
	Normalized Yield	18.2	± 1.1
$e^+e^- \rightarrow \tau^+\tau^-$	Cutoff m_0	1887.0 MeV	Fixed
	Curvature c	6.4	± 3.8
	Power p	0.40	± 0.15
	Normalized Yield	36.0	± 1.5
$D\bar{D}$ -pairs	Cutoff m_0	1887.0 MeV	Fixed
	Curvature c	-18.7	± 3.1
	Power p	0.60	± 0.10
	Normalized Yield	28.9	1.0
$D^+ \rightarrow \pi^+ K_L$	Cutoff m_0	1887.0 MeV	Fixed
	Curvature c	-47.0	± 3.6
	Power p	0.80	± 0.092
	1st Gaussian \bar{x}	1869.54 MeV	± 0.25 MeV
	1st Gaussian σ	1.27 MeV	± 0.23 MeV
	Fraction in 1st Gaussian	0.10	± 0.018
	Normalized Yield	8.86	± 0.32
$D^+ \rightarrow \pi^+ \pi^0$	Primary Gaussian \bar{x}_1	1689.53 MeV	± 0.047 MeV
	Primary Gaussian σ_1	1.39 MeV	± 0.058 MeV
	Secondary Gaussian \bar{x}_2	1869.83 MeV	± 0.20 MeV
	Secondary Gaussian σ_2	4.00 MeV	± 0.28 MeV
	Fraction in First Gaussian	0.73	± 0.036
	Normalized Yield	4.52	± 0.096
$D^+ \rightarrow \tau^+ \nu_\tau$	Primary Gaussian \bar{x}_1	1689.49 MeV	± 0.045 MeV
	Primary Gaussian σ_1	1.34 MeV	± 0.056 MeV
	Secondary Gaussian \bar{x}_2	1869.66 MeV	± 0.15 MeV
	Secondary Gaussian σ_2	3.63 MeV	± 0.20 MeV
	Fraction in First Gaussian	0.69	± 0.036
	Fraction of signal peak	0.055	± 0.011

We will fit this using an ARGUS function in exactly the same way as we have fit the $e^+e^- \rightarrow \tau^+\tau^-$, the $e^+e^- \rightarrow \psi'\gamma$ and $D\bar{D}$ from Monte Carlo, but we will allow all parameters to float. This will then be included in the total fit which we will run on the data along with all the other fixed contributions from Monte Carlo and the floating signal contribution.

Table 6.3: The parameters for the continuum ARGUS fit and the signal peak yield obtained from the fit to data.

Continuum	Cutoff m_0	1885.0 MeV	± 1.01 MeV
	Curvature c	-9.22	± 2.73
	Power p	1.00	± 0.17
	Normalized Yield	360.	$\pm 22.$
Signal Peak	Yield	79.2	± 10.9
$D^+ \rightarrow \mu^+\nu_\mu$	Yield	74.8	± 10.4

6.4 Combined Fit

The combined fit is shown in two Figures in order to better show the various contributions to the fit. This is obtained using all of the parameters from Tables 6.1 and 6.2 as fixed and allowing the continuum parameters to float freely. Figure 6.8 has a linear y -axis, which clearly shows the signal peak while Figure 6.9 has a logarithmic y -axis, allowing the different background components to be more easily differentiated from one another. The contributions, in ascending order, are: generic $D\bar{D}$ (green dashed) $e^+e^- \rightarrow \psi'\gamma$ (orange solid), $e^+e^- \rightarrow \tau^+\tau^-$ (gray dashed), continuum (blue solid), $D^+ \rightarrow \pi^+K_L$ (purple dashed), $D^+ \rightarrow \pi^+\pi^0$ (yellow solid) and signal peak (red solid). The signal peak, we should note, includes a contribution from both the $D^+ \rightarrow \mu^+\nu_\mu$ and $D^+ \rightarrow \tau^+\nu_\tau$, where the $D^+ \rightarrow \tau^+\nu_\tau$ portion makes

up $5.4056\% \pm 0.1128\%$ of the peak.

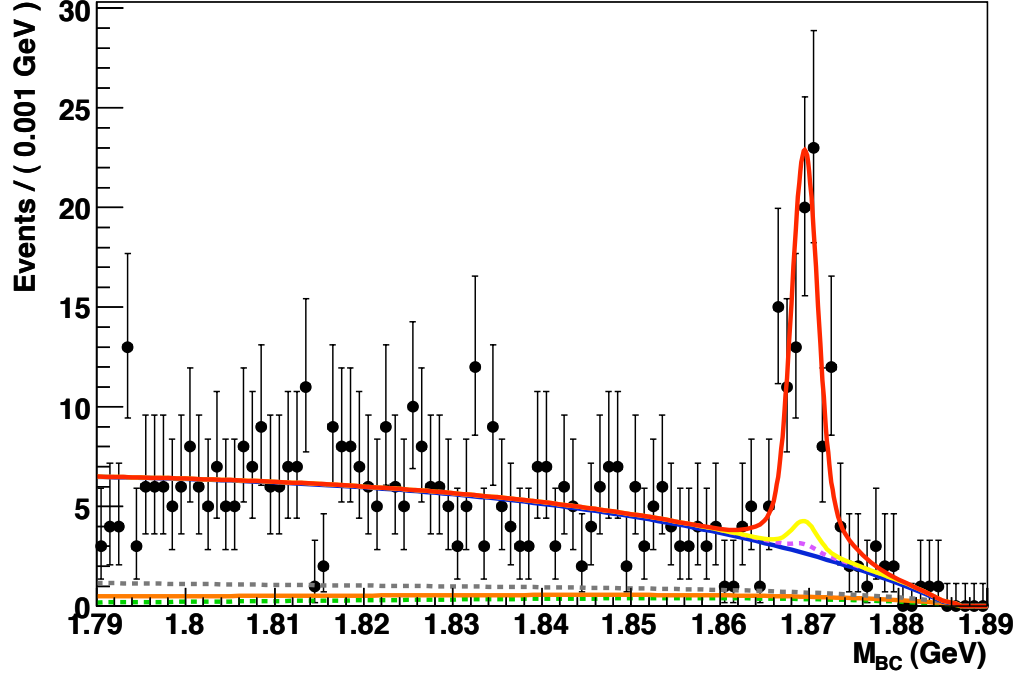


Figure 6.8: A fit of data using the combined information from the backgrounds and signal. In ascending order, the contributions are: DD (green dashed) $e^+e^- \rightarrow \psi'\gamma$ (orange solid), $e^+e^- \rightarrow \tau^+\tau^-$ (gray dashed), continuum (blue solid), $D^+ \rightarrow \pi^+K_L$ (purple dashed), $D^+ \rightarrow \pi^+\pi^0$ (yellow solid) and signal peak (red solid).

The final parameters determined from the fit are shown in Table 6.3. The continuum is clearly, as is obvious from the plot and the table, the largest single source of background. With the $D^+ \rightarrow \tau^+\nu_\tau$ contribution of the signal peak removed, the final raw $D^+ \rightarrow \mu^+\nu_\mu$ yield is 75.08 ± 10.42 .

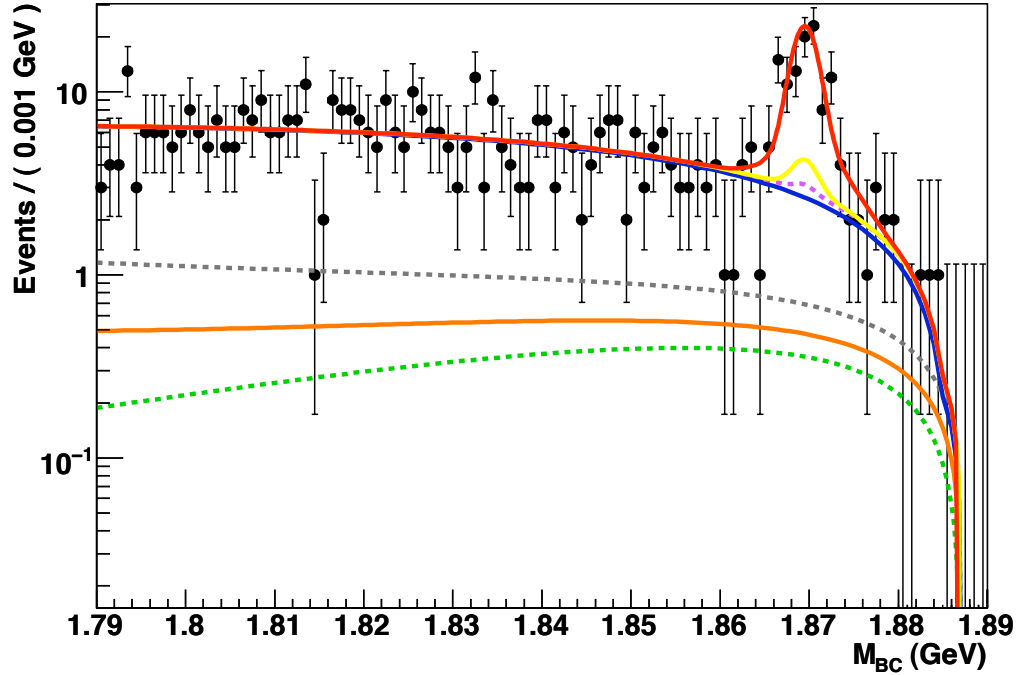


Figure 6.9: A fit of data using the combined information from the backgrounds and signal. To help illustrate the background components, the y -axis is logarithmic. In ascending order, the contributions are: $D\bar{D}$ (green dashed) $e^+e^- \rightarrow \psi'\gamma$ (orange solid), $e^+e^- \rightarrow \tau^+\tau^-$ (gray dashed), continuum (blue solid), $D^+ \rightarrow \pi^+K_L$ (purple dashed), $D^+ \rightarrow \pi^+\pi^0$ (yellow solid) and signal peak (red solid).

6.5 Fitting $D \rightarrow K^-\pi^+\pi^+$

We fit the $D^+ \rightarrow K^-\pi^+\pi^+$ distribution using a combination of a double Gaussian for the peak, plus an ARGUS shape for the background. All parameters are allowed to float (with the exception of the cut-off for the ARGUS shape, which is fixed at the beam energy) and the result of the fit is shown (on a log-scale plot) in Figure 6.10. The parameters from the fit are shown in Table 6.4.

Unlike the fit for $D^+ \rightarrow \mu^+\nu_\mu$, the fit for $D^+ \rightarrow K^-\pi^+\pi^+$ comes straight from

Table 6.4: The parameters for the $D^+ \rightarrow K^- \pi^+ \pi^+$ fit from data.

ARGUS Shape	Cutoff m_0	1887.0 MeV	Fixed
	Curvature c	-6.32	± 1.21
	Power p	0.50	± 0.003
	Normalized Yield	1815.	$\pm 50.$
Peak	Primary Gaussian \bar{x}_1	1869.33 MeV	± 0.023 MeV
	Primary Gaussian σ_1	1.30 MeV	± 0.020 MeV
	Secondary Gaussian \bar{x}_2	1872.56 MeV	± 0.45 MeV
	Secondary Gaussian σ_2	3.92 MeV	± 0.31 MeV
	Fraction in First Gaussian	0.89	± 0.012
	Peak Yield	5008.	$\pm 76.$

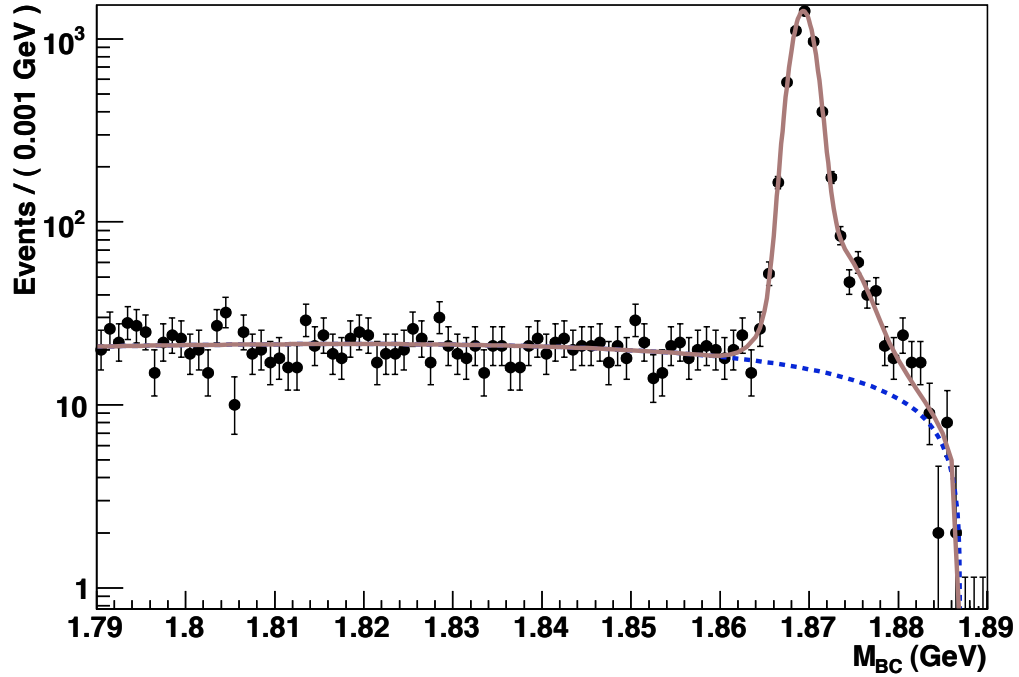


Figure 6.10: A fit to data of the $D^+ \rightarrow K^- \pi^+ \pi^+$ reference mode, as a combination of an ARGUS background plus a signal peak which is the sum of a Gaussian and a Crystal Ball function.

data; there is sufficient data to make using Monte Carlo for any portion of it unnecessary.

Chapter 7

Systematic Uncertainties

7.1 Overview

The measurement of the branching fraction of $D^+ \rightarrow \mu^+ \nu_\mu$ is dominated by the statistical uncertainty caused by the low number of events ultimately found. Furthermore, most of the systematic errors that occur in the analysis will be as a result of the basic reconstruction technique (involving the improved reconstruction of the other side). They will therefore cancel out when the ratio is taken between the yield of the $D^+ \rightarrow \mu^+ \nu_\mu$ and the $D^+ \rightarrow K^- \pi^+ \pi^+$ measurements. There are, however, still some few additional sources of systematic error which we will now catalog and whose magnitude we will quantify.

7.2 Corrections

A number of systematic studies have previously been done regarding systematic corrections for track-finding efficiencies for different types of charged particles, as well as K_S and π^0 candidates [29, 18]. Since the use of these will chiefly involve the tracks and showers of the D^- candidate, which will be the same for both $D^+ \rightarrow \mu^+ \nu_\mu$ and $D^+ \rightarrow K^- \pi^+ \pi^+$, using these is chiefly a historical relic of wanting to have consistency with other analyses; Including them or not does not lead to any change in the final yield.

7.3 Fitting

In making our final fit of the data in section 6.4 we allowed only the parameters of the continuum ARGUS shape and the yield of the signal peak to float, fixing all the others. We now consider the effects of varying these various fixed parameters.

The parameters were all obtained from functional fits to Monte Carlo samples, and in order to obtain a systematic error we will now vary each of these parameters by 1σ , as defined by Tables 6.2 and 6.1. The effect of varying any given one of these parameters is small, and the largest effect comes from varying the parameters of the double Gaussian for the signal peak; our result is most sensitive to the width of the two Gaussians and their relative contribution. “Most sensitive” is a relative term, however, as these do not change the efficiency-corrected yield by more than 0.5%.

Because we did not allow the yields of the backgrounds to float in our final fit, we will actually allow these parameters to vary by more than the 1σ given in Table `reftable:backgroundParameters` (increasing this to 2–3 σ). Doing so introduces no significant change in the final yield, showing that our result is robust. We add the contributions from all the changes of the fitting parameters in quadrature and assess the systematic uncertainty due to fitting to be 1.1%.

7.4 Selection Requirements

Not all of the selection requirements are precisely the same for the $D^+ \rightarrow K^- \pi^+ \pi^+$ and $D^+ \rightarrow \mu^+ \nu_\mu$ measurements and it is therefore useful to look at how the efficiency-corrected yield of the $D^+ \rightarrow \mu^+ \nu_\mu$ would vary if these other cuts are

allowed to vary. In principle such a variation would affect the signal efficiency and distribution, the background yield and distribution, and the data yield and distribution.

Note that changing a given criterion affects several things: the signal efficiency, the background yields and distributions, and of course the data yield and distribution. The distributions of the backgrounds (as used for purposes of fitting) and their variation is covered in Section 7.3, so for the purposes of this evaluation, we will be determining only the change in yields and measure their effect on the final efficiency-corrected $D^+ \rightarrow \mu^+ \nu_\mu$ yield.

The possible selection criteria to be examined from Chapter 3 are $\Delta E_{\text{o.s.}}$, $MM_{\text{s.s.}}^2$, m_ν^2 , $\cos \theta(\vec{p}_{\text{miss}})$ and the cut on the energy deposition in the CC matched to the μ^+ track. The cuts for these are all summarized in Table 3.1. The different cuts were each varied by roughly 1% of their range in the following manner:

- The cut on the $\cos \theta(\vec{p}_{\text{miss}})$ was varied by ± 0.01
- The cut on the energy deposited in the CC was varied by ± 3 MeV
- The selection window for $\Delta E_{\text{o.s.}}$ was shifted up and down by 0.01 GeV, i.e. to a range of -0.059 – 0.51 GeV and -0.061 – 0.49 GeV, respectively
- The selection windows for $MM_{\text{s.s.}}^2$ and m_ν^2 were each shifted up and down by $0.02 \text{ GeV}^2/c^4$ in the same manner as the selection window of $\Delta E_{\text{o.s.}}$

The deviations from the eight possible variation scenarios are added in quadrature in order to give a conservative systematic uncertainty assessment of 2.1% from our selection criteria.

7.5 Tracking

The systematic uncertainties associated with tracking of charged particles are well known in the CLEO-c environment [30]. Furthermore, these will be the same for the majority of the tracks for $D^+ \rightarrow \mu^+ \nu_\mu$ and $D^+ \rightarrow K^- \pi^+ \pi^+$ events, thus canceling when we calculate our ratio. However, there is still the tracking systematic error for our signal μ^\pm , for which we assign an uncertainty of 1.0%.

7.6 Hadronic Branching Fraction Ratio

There is a final systematic error associated with the uncertainty on the well-known $D^+ \rightarrow K^- \pi^+ \pi^+$ branching fraction. We use the combined statistical and systematic error from the CLEO-c measurement of 2.2% as our systematic uncertainty from this source. [19].

Table 7.1: Systematic Uncertainties

<i>Source</i>	<i>Uncertainty (%)</i>
Tracking	1.0
Fitting	1.1
Selection Requirements	2.1
$D^+ \rightarrow K^- \pi^+ \pi^+$ branching fraction	2.2

7.7 Summary

The three main sources of systematic error are shown in table 7.1. For our final value we will add them in quadrature giving a total systematic uncertainty of 3.4%.

Chapter 8

Results

Using the fitting technique described in chapter 6, we were able to obtain a value for the raw yield of $D^+ \rightarrow \mu^+ \nu_\mu$ events. The efficiency-corrected yields are shown in Table 8.1, which show both the yields for $D^+ \rightarrow \mu^+ \nu_\mu$ and $D^+ \rightarrow K^- \pi^+ \pi^+$.

Table 8.1: The efficiency corrected yields for $D^+ \rightarrow K^- \pi^+ \pi^+$ and $D^+ \rightarrow \mu^+ \nu_\mu$.

Decay	Efficiency Corrected Yield	Relative Branching Fraction
$D^+ \rightarrow K^- \pi^+ \pi^+$	$(1.45 \pm 0.01) \times 10^5$	1
$D^+ \rightarrow \mu^+ \nu_\mu$	621 ± 86	$(4.27 \pm 0.60) 10^{-3}$

From this we obtain the total branching fraction $\mathcal{B}(D^+ \rightarrow \mu^+ \nu_\mu) = (3.90 \pm 0.55_{stat} \pm 0.13_{syst}) \times 10^{-4}$. In order to obtain a value for f_{D^+} , we then use Equation 1.6 where we use the measured total width of D^+ . We can also make the assumption that the top left 2×2 portion of the CKM matrix is unitary and use this fact to substitute V_{us} for V_{cd} (since the former is known to much greater precision than the latter). We use a value of 0.2255 ± 0.0019 for V_{us} and $(1040 \pm 7) \times 10^{-15}$ s for the D^+ life-time [31]. From this we obtain $f_{D^+} = (209.7 \pm 14.6_{stat} \pm 3.5_{syst})$ MeV.

BIBLIOGRAPHY

- [1] G. P. Lepage, “Lattice QCD for Novices,” in *Proceedings of HUGS 98*, 1998.
- [2] C. T. H. Davies *et al.*, “High-precision lattice QCD confronts experiment,” *Phys. Rev. Lett.*, vol. 92, p. 022001, 2004.
- [3] T. Meyer, “Identifying Hadronic Splitoffs in CLEO Data: SplitoffProd.” <https://www.lepp.cornell.edu/cleo3/development/src/SplitoffProd/Doc>, 2001.
- [4] J. Joyce, *Finnegans Wake*. New York: Penguin Books, 1999.
- [5] L. C. C. L. Dodgson), *Through the Looking-Glass, and What Alice Found There*. Macmilan, 1871.
- [6] C. Aubin *et al.*, “Charmed meson decay constants in three-flavor lattice QCD,” *Phys. Rev. Lett.*, vol. 95, p. 122002, 2005.
- [7] M. Artuso *et al.*, “Improved measurement of $B(D^+ \rightarrow \mu^+\nu)$ and the pseudoscalar decay constant f_{D^+} ,” *Phys. Rev. Lett.*, vol. 95, p. 251801, 2005.
- [8] E. Follana *et al.*, “Highly improved staggered quarks on the lattice, with applications to charm physics,” *Phys. Rev.*, vol. D75, p. 054502, 2007.
- [9] E. Follana, C. T. H. Davies, G. P. Lepage, and J. Shigemitsu, “High Precision determination of the π , K , D and D_s decay constants from lattice QCD,” *Phys. Rev. Lett.*, vol. 100, p. 062002, 2008.
- [10] J. D. Richman and P. R. Burchat, “Leptonic and semileptonic decays of charm and bottom hadrons,” *Rev. Mod. Phys.*, vol. 67, pp. 893–976, Oct 1995.
- [11] M. E. Peskin and D. V. Schroeder, *An Introduction to quantum field theory*. Addison-Wesley, 1995. Reading, USA: Addison-Wesley (1995) 842 p.
- [12] F. Sauli, “Principles of Operation of Multiwire Proportional and Drift Chambers.” CERN-77-09, 1977.
- [13] W. M. Yao *et al.*, “Review of particle physics,” *J. Phys.*, vol. G33, pp. 1–1232, 2006.

- [14] M. Artuso *et al.*, “The CLEO RICH detector,” *Nucl. Instrum. Meth.*, vol. A554, pp. 147–194, 2005.
- [15] C. Park and E. Thorndike, “A Study of $D \rightarrow e^+ X$ Decays.” CBX 05-73, 2005.
- [16] L. Fields, “Trkman-c.” CBX04-37, 2004.
- [17] N. E. Adam *et al.*, “Absolute branching fraction measurements for D^+ and D^0 inclusive semileptonic decays,” *Phys. Rev. Lett.*, vol. 97, p. 251801, 2006.
- [18] R. Gray, *Semileptonic Decays $D^+ \rightarrow \eta^{(\prime)} \ell^+ \nu$ with Generic Reconstruction of Fully Hadronic D^+ and D^0 Decays*. PhD thesis, Cornell University, Ithaca, New York, 2008.
- [19] S. Dobbs *et al.*, “Measurement of Absolute Hadronic Branching Fractions of D Mesons and $e^+e^- \rightarrow D\bar{D}$ Cross Sections at the $\psi(3770)$,” *Phys. Rev.*, vol. D76, p. 112001, 2007.
- [20] D. Besson *et al.*, “Measurement of $\sigma(e^+e^- \rightarrow \psi(3770) \rightarrow \text{hadrons})$ at $E_{CM} = 3773$ MeV,” *Phys. Rev. Lett.*, vol. 96, p. 092002, 2006.
- [21] T. Sjostrand, *PYTHIA 5.7 and JETSET 7.4: Physics and manual*, 1995.
- [22] H. Albrecht *et al.*, “SEARCH FOR HADRONIC $b \rightarrow u$ DECAYS,” *Phys. Lett.*, vol. B241, pp. 278–282, 1990.
- [23] W. Verkerke and D. Kirkby, *The RooFit toolkit for data modeling*, 2003.
- [24] G. S. Adams *et al.*, “Measurement of $\Gamma(ee)(J/\psi)$, $\Gamma(\text{tot})(J/\psi)$, and $\Gamma(ee)(\psi(2S)) / \Gamma(ee)(J/\psi)$,” *Phys. Rev.*, vol. D73, p. 051103, 2006.
- [25] S. Jadach and Z. Was, “Koralb: An Upgrade to version 2.4,” *Comput. Phys. Commun.*, vol. 85, pp. 453–462, 1995.
- [26] Q. He *et al.*, “Comparison of $D \rightarrow K_s^0 \pi$ and $D \rightarrow K_L^0 \pi$ Decay Rates,” *Phys. Rev. Lett.*, vol. 100, p. 091801, 2008.
- [27] R. Brun and F. Rademakers, “ROOT: An object oriented data analysis framework,” *Nucl. Instrum. Meth.*, vol. A389, pp. 81–86, 1997.
- [28] E. D. Bloom and C. Peck, “Physics with the Crystal Ball Detector,” *Ann. Rev. Nucl. Part. Sci.*, vol. 33, pp. 143–197, 1983.

- [29] N. Adam and L. Gibbons, “A Study of the Form Factors and CKM Matrix Elements of the Exclusive Semileptonic Decays $D^0 \rightarrow K^- e^+ \nu$, $D^0 \rightarrow \pi e^+ \nu$, $D^+ \rightarrow \bar{K}^0 e^+ \nu$, and $D^+ \rightarrow \pi^0 e^+ \nu$.” CBX 07-07, 2007.
- [30] S. Stroiney, A. Ryd, W. Sun, P. Onyisi, D. Cassel, “Determination of Tracking Efficiencies (For D Hadronic Branching Fraction Analysis).” CBX 06-29b, 2006.
- [31] C. Amsler *et al.*, “Review of particle physics,” *Phys. Lett.*, vol. B667, p. 1, 2008.